A theoretical foundation for multi-scale regular vegetation patterns

Corina E. Tarnita[1,2,*], Juan A. Bonachela[3,*], Efrat Sheffer[4], Jennifer A. Guyton[1], Tyler C. Coverdale[1], Ryan A. Long[5], Robert M. Pringle[1,2]

[1] Department of Ecology & Evolutionary Biology, Princeton University, Princeton, NJ 08544, USA

[2] Mpala Research Center, Box 555, Nanyuki, Kenya

[3] Marine Population Modeling Group, Department of Mathematics and Statistics, University of Strathclyde, Glasgow, G1 1XH, Scotland, UK

[4] The R.H. Smith Institute for Plant Sciences and Genetics in Agriculture, The Faculty of Agriculture, Hebrew University of Jerusalem, Rehovot 7610001, Israel

[5] Department of Fish and Wildlife Services, University of Idaho, Moscow, ID 83844

[*] Equal contribution.

Self-organized regular vegetation patterns are widespread[1] and thought to mediate ecosystem functions such as productivity and robustness[2-4], but the mechanisms underlying their origin and maintenance remain disputed. Particularly controversial are landscapes of overdispersed (evenly spaced) elements (Fig. 1), such as North American Mima mounds, Brazilian *murundus*, South African *heuweltjies*, and, famously, Namibian fairy circles (FCs)[5-13]. Two competing hypotheses are currently debated. On the one hand, models of scale-dependent feedbacks (SDF), whereby plants facilitate neighbors while competing with distant individuals, can reproduce various regular patterns identified in satellite imagery[1,14,15]. Due to its deep theoretical roots and apparent generality, SDF is widely viewed as a unifying and near-universal principle of regular-pattern formation[1,16,17] despite scant empirical evidence[18]. On the other hand, many overdispersed vegetation patterns worldwide have been attributed to subterranean ecosystem engineers such as termites, ants, and rodents[3,4,7,19-22]. Although potentially consistent with territorial competition[19-21,23,24], this interpretation has been challenged theoretically and empirically[11,17,24-26] and (unlike SDF) lacks a unifying dynamical theory, fueling skepticism about its plausibility and generality[5,9-11,16-18,24-26]. Here we provide a general theoretical foundation for self-organization of social-insect colonies, validated using data from four continents, demonstrating that intraspecific competition between territorial animals can generate the large-scale hexagonal regularity of these patterns. However, this mechanism is not mutually exclusive with SDF. Using Namib-Desert FCs as a case study, we present novel field data showing that these landscapes exhibit multi-scale patterning—previously undocumented in this system—that cannot be explained by either mechanism in isolation. These multi-scale patterns and other emergent properties, such as enhanced resistance to and recovery from drought, instead arise from dynamic feedbacks in our theoretical framework that couples both mechanisms. The potentially global extent of animal-induced regularity in vegetation—which can modulate other patterning processes in functionally important ways—underscores the need to integrate multiple mechanisms of ecological self-organization[27].

Hypotheses about the origin of regularly patterned (i.e., spatially periodic with characteristic cluster size) landscapes are typically presented as strict alternatives, leading to strident and long-lasting debates[5-12,17,22,28]. The Namib FCs provide a fascinating case in point. FCs are bare discs 2–35m wide surrounded by rings of tall perennial grasses, found in sandy desert soils along a sliver of southwestern Africa (Figs. 1f, 4a)[7,28]. Recently, Juergens[7] documented strong correlations between FCs and sand-termite (*Psammotermes allocerus*) activity and proposed a conceptual model in which termites engineer FCs by killing plants, thereby creating bare patches that concentrate moisture[7,8]. This hypothesis elicited a barrage of counterarguments advocating SDF[9-13,18], with debate revolving heavily around the large-scale hexagonal distribution of FCs (each FC has ~6 neighbors on average). It has been argued, for example, that social insects "are not able to create such extremely ordered, and at the same time large-scale homogeneous patterns," leaving SDF as "the most reasonable working hypothesis"[17]. Parallel disputes simmer over the origins of other regular vegetation patterns worldwide, pitting soil fauna versus SDF[5].

Although often implicitly presented as alternatives, these two mechanisms are not mutually exclusive. Here we reconcile these competing perspectives by theoretically integrating both mechanisms for the first time and testing their predictions against empirical observations. First, we develop a dynamic spatial model to characterize the population dynamics and territorial behavior of a generic soil-nesting social-insect population, showing that intraspecific competition can theoretically generate large-scale hexagonal patterns found in termite mound-fields[3], *heuweltjies*[22], *murundus*[5], and FCs[10]. Second, to explore the dynamic interaction and emergent effects of multiple simultaneous self-organization processes, we couple this faunal model to one of SDF-driven vegetation self-organization. We illustrate the power of this merged framework using Namib FCs as a case study: by parameterizing our merged model specifically for that system and testing its predictions against remotely sensed imagery and novel field observations, we show that the interplay of both mechanisms (a) characterizes the vegetation patterns of Namib FC landscapes more completely than either mechanism can in isolation, and (b) predicts the emergence of features in these landscapes that have escaped the notice of prior investigators. This analysis moves beyond dichotomous debates to explore the multi-trophic dynamics and feedbacks that underpin multi-scale regular patterning in complex ecosystems.

To model social-insect self-organization, we used a spatially explicit model of colony dynamics in a discrete landscape, parameterized from the literature (Extended Data Table 1). Colonies build central nests and forage outwards to acquire resources to fuel colony-population growth and survival. Mature (established) colonies produce alates (reproductive future queens/kings) that disperse randomly throughout our simulated landscapes and attempt to initiate new colonies. Resource availability is constant and uniformly distributed. When the expanding foraging areas of neighboring colonies overlap, conflicts ensue via territorial aggression (Extended Data Fig. 1a), as is common among social insects[29]. Conflict outcomes depend probabilistically on relative colony size: larger colonies are more likely to eliminate smaller ones, but similar-sized colonies coexist, whereupon a shared boundary emerges (Extended Data Fig. 1b). These conflicts are the primary cause of young-colony mortality (and are intensified by environmental stressors such as drought), while mature colonies have additional probabilistic death rates consistent with typical lifespans reported in the literature.

Although this system is intrinsically dynamic due to continual births and deaths of colonies (Supplementary Video 1), the quantities of interest eventually reach stationarity (fluctuating around a well-defined constant average) (Extended Data Fig. 2a,b). We can thus explore how this stationary state depends on resource availability. Mean density and population

size of mature colonies increased—and mean nest diameter, foraging area, and nearest-neighbor distance decreased—with increasing resource density (Extended Data Fig. 2c-f). This occurred because colonies in resource-rich environments require smaller foraging areas to achieve a given increase in population size. Moreover, colony sizes in low-resource environments were always food-limited (Extended Data Fig. 2f), consistent with prior experimental work[20].

We quantified predicted nest distributions (Fig. 1a) using standard point-pattern analyses: Voronoi diagrams, pair-correlation function, and Ripley's *L* (see Methods). Regardless of resource density, mature nests in our simulations were regularly and hexagonally overdispersed, with ~6 neighbors on average (Fig. 1g-i, Extended Data Fig. 2g). In contrast, immature (typically short-lived) colonies were randomly distributed or clumped, as observed in many ant and termite populations[20,21,25,26]. These theoretical results correspond well with our analyses of empirical nest distributions for diverse social-insect species from Africa, North and South America, and Australia (Fig. 1, Extended Data Fig. 3,4, Supplementary Text 4.1). Although the degree of hexagonal regularity differs somewhat among sites due to variable topo-edaphic and floristic uniformity, the repeated emergence of such patterns in diverse contexts worldwide—despite the ubiquity of environmental heterogeneity—affirms the generality of the phenomenon[27].

Our general social-insect model also reproduced the spatial distribution of Namibian FCs[10] (Fig. 1f-i, Extended Data Figs. 3,4), showing that the large-scale hexagonal pattern of mature circles and the small-scale heterogeneity of immature circles[22,28] can theoretically be explained by termite activity, contrary to recent arguments[17]. However, this finding does not exclude the possibility that SDF concurrently drives vegetation patterning in this arid system. Therefore, we next developed a theoretical framework incorporating simultaneous social-insect and vegetation self-organization and applied it to the Namib FC system. In the model, termites increase grass mortality on/around nest sites[7,8] and forage on dead biomass in the surrounding matrix. To model vegetation (parameterized as a generic tussock grass, like the *Stipagrostis* spp. bushman-grasses that dominate the Namib), we modified a widely-used partial-differential-equation SDF model[15] previously applied to Namib FCs[9,10] by (a) incorporating stochastic rainfall, based on 10-year records from NamibRand Nature Reserve (Extended Data Fig. 5) and (b) allowing for asymmetric root-biomass growth and water uptake in areas with higher moisture concentrations. We parameterized this model using appropriate values from the literature (Extended Data Tables 1,2).

In this coupled model, termites and vegetation dynamically self-organize and interact. Bare FC discs with elevated soil moisture emerge around nests under arid conditions (Fig. 2, Extended Data Fig. 6). If rainfall increases, however, plant regeneration outpaces termite-induced mortality, and FCs revegetate (Extended Data Fig. 7), possibly explaining why FCs are absent from *Psammotermes* nests in mesic regions[17] (moisture-mediated plasticity in termite-foraging behavior has been suggested as another explanation[22]). Asymmetric root-biomass growth and water uptake by plants surrounding the moisture-rich bare discs (Fig. 2d,e) promotes emergence of dense, tall grass rings like the FC "perennial belts"[7] (Fig. 2b,c,f), an important feature not predicted by prior SDF models[9,10]. FC life cycles emerge in our model, driven by colony establishment, growth, and death (Fig. 3, Supplementary Video 2). FCs emerge quickly following colony establishment, but disappear more slowly after colonies die (Fig. 3k-p) as grasses invade and eventually fill the bare patches (Fig. 3, Extended Data Fig. 6e,f). The weakly bimodal distribution of lifespans ranges broadly from <5 to >165 years (Extended Data Fig. 8), with a peak at <15y and another at ~30–60y, consistent with the existing range of empirical estimates[6,7,22]. The results above accord with published empirical data and satisfy quantitative

criteria proposed to characterize the Namib FC system[6,7,12,17,22].

Our coupled model also predicts a previously unrecognized feature of the Namib landscape. Prior studies have focused exclusively on the FCs and largely ignored the matrix in between. In our model, SDF induces dynamic self-organization of the matrix vegetation, but at smaller spatial scales more compatible with ecohydrologically realistic grass-water feedback distances (Supplementary Video 3). Following wet seasons, small, regular clumps of matrix vegetation emerge, interspersed with larger, randomly distributed clumps (Fig. 2c). These larger clumps are rare in the SDF-only model without termites, but arise in the coupled model from small-scale soil-moisture variability in the matrix (Fig. 2d; consistent with data[22])—itself a ripple effect created by the FCs (Extended Data Fig. 6). To evaluate these theoretical predictions, we photographed NamibRand matrix-vegetation distributions from 10-m height in February 2015 and characterized both model-predicted and observed patterns using Fourier-transform analyses (see Methods). We found strong agreement between model outputs and field data (Fig. 4).

Thus, by treating SDF and faunal engineering as complementary processes rather than competing alternatives, our model achieves the most comprehensive and realistic description of this system to date. Whereas prior SDF models can reproduce only the formation and qualitative dynamics of hexagonally patterned bare discs[9,10,13], our incorporation of termite self-organization and its feedbacks with SDF yields emergent properties absent from prior models but present in the real landscape, including vegetation size structure and the hitherto undocumented small-scale patterning of matrix vegetation.

Finally, we asked how the interplay of faunal engineering and SDF influenced ecosystem responses to climatic perturbations. Simulated drought (20% reduction in rainfall sustained over 1, 5, or 10 years) reduced system-wide vegetation biomass, but these losses were smaller (i.e., landscapes more drought-resistant) when termites were present. This occurred because the densely vegetated rings and large matrix tussocks generated by the termite-SDF interaction are more drought-resistant and persist after the small matrix patches disappear. Returning rainfall to baseline after drought enabled regeneration of matrix vegetation in both systems; however, recovery occurred faster in the coupled termite-SDF system, because the perennial rings and large matrix clumps act as drought refugia and post-drought sources (Supplementary Video 4). Thus, plant-water-consumer feedbacks sustain the productivity of the Namib by enhancing both its resistance to and recovery from climatic perturbations, as recently hypothesized[7].

Collectively, our results not only show that interactions among social-insect colonies and vegetation can explain a diverse global suite of regular spatial patterns, but also underscore the potential for co-occurrence and complementarity among distinct patterning mechanisms in generating multi-scale regularity[4,30]. This highlights the need to focus theoretical and empirical effort on the ways in which multiple mechanisms interact across scales to structure ecosystems[27]. Advances in remote sensing have buoyed the study of ecological self-organization, but remain insufficient to reveal small-scale patterns. Likewise, evaluating the causes of particular patterns and elucidating multi-mechanism feedbacks will require manipulative field experimentation and 8and competitive dynamics of cryptic ecosystem-engineer species; the ways in which plants and SDF respond to bioturbation and climatic variability; and the movement of water through soil in different environmental contexts. Equipped with such knowledge, it may be possible to identify reliable signatures of different mechanisms and specify the scales at which they act and interact.

1. Rietkerk, M. & van de Koppel, J. Regular pattern formation in real ecosystems. *TREE* **23,** 169–175 (2008).
2. Scheffer, M. *et al.* Early-warning signals for critical transitions. *Nature* **461,** 53–59 (2009).
3. Pringle, R. M., Doak, D. F., Brody, A. K., Jocqué, R. & Palmer, T. M. Spatial pattern enhances ecosystem functioning in an African savanna. *PLoS Biol.* **8,** e1000377 (2010).
4. Bonachela, J. A. *et al.* Termite mounds can increase the robustness of dryland ecosystems to climatic change. *Science* **347,** 651–655 (2015).
5. Cramer, M. D. & Barger, N. N. Are mima-like mounds the consequence of long-term stability of vegetation spatial patterning? *Palaeogeogr. Palaeocl. Palaeoecol.* **409,** 72–83 (2014).
6. Tschinkel, W. R. The life cycle and life Span of Namibian fairy circles. *PLoS ONE* **7,** e38056 (2012).
7. Juergens, N. The biological underpinnings of Namib Desert fairy circles. *Science* **339,** 1618–1621 (2013).
8. Vlieghe, K., Picker, M., Ross-Gillespie, V. & Erni, B. Herbivory by subterranean termite colonies and the development of fairy circles in SW Namibia. *Ecol. Entomol.* **40,** 42–49 (2015).
9. Zelnik, Y. R., Meron, E. & Bel, G. Gradual regime shifts in fairy circles. *Proc. Natl. Acad. Sci. USA* **112,** 12327–12331 (2015).
10. Getzin, S. *et al.* Adopting a spatially explicit perspective to study the mysterious fairy circles of Namibia. *Ecography* **38,** 1–11 (2015).
11. Getzin, S. *et al.* Discovery of fairy circles in Australia supports self-organization theory. *Proc. Natl. Acad. Sci. USA* **113,** 3551–3556 (2016).
12. Cramer, M. D. & Barger, N. N. Are Namibian 'fairy circles' the consequence of self-organizing spatial vegetation patterning? *PLoS ONE* **8,** e70876 (2013).
13. Fernandez-Oto, C., Tlidi, M., Escaff, D. & Clerc, M. G. Strong interaction between plants induces circular barren patches: fairy circles. *Phil. Trans. Roy. Soc. A* **372,** 20140009 (2014).
14. Meron, E. Modeling dryland landscapes. *Math. Model. Nat. Phenom.* **6,** 163–187 (2011).
15. Gilad, E., Hardenberg, von, J., Provenzale, A., Shachak, M. & Meron, E. A mathematical model of plants as ecosystem engineers. *J. Theor. Biol.* **244,** 680–691 (2007).
16. Deblauwe, V., Couteron, P., Lejeune, O., Bogaert, J. & Barbier, N. Environmental modulation of self-organized periodic vegetation patterns in Sudan. *Ecography* **34,** 990–1001 (2011).
17. Getzin, S. *et al.* Clarifying misunderstandings regarding vegetation self-organisation and spatial patterns of fairy circles in Namibia: a response to recent termite hypotheses. *Ecol. Entomol.* **40,** 669–675 (2015).
18. Tschinkel, W. R. Experiments testing the causes of Namibian fairy circles. *PLoS ONE* **10,** e0140099 (2015).
19. Levings, S. C. & Traniello, J. Territoriality, nest dispersion, and community structure in ants. *Psyche* (1981).
20. Korb, J. & Linsenmair, K. E. The causes of spatial patterning of mounds of a fungus-cultivating termite: results from nearest-neighbour analysis and ecological studies. *Oecologia* **127,** 324–333 (2001).
21. Grohmann, C., Oldeland, J., Stoyan, D. & Linsenmair, K. E. Multi-scale pattern analysis

of a mound-building termite species. *Insect. Soc.* **57,** 477–486 (2010).
22. Juergens, N. *et al.* Weaknesses in the plant competition hypothesis for fairy circle formation and evidence supporting the sand termite hypothesis. *Ecol. Entomol.* **40,** 661–668 (2015).
23. Laurie, H. Optimal transport in central place foraging, with an application to the overdispersion of heuweltjies. *S. Afr. J. Sci.* **98,** 141–146 (2002).
24. Ryti, R. T. & Case, T. J. The role of neighborhood competition in the spacing and diversity of ant communities. *Am. Nat.* **139,** 355–374 (1992).
25. Schuurman, G. & Dangerfield, J. M. Dispersion and abundance of *Macrotermes michaelseni* colonies: a limited role for intraspecific competition. *J. Trop. Ecol.* **13,** 39–49 (1997).
26. Adams, E. S. & Tschinkel, W. R. Spatial dynamics of colony interactions in young populations of the fire ant *Solenopsis invicta*. *Oecologia* **102,** 156–163 (1995).
27. Pringle, R. M. & Tarnita, C. E. Spatial self-organization of ecosystems: integrating multiple mechanisms of regular-pattern formation. *Annu. Rev. Entomol.* **62,** in press (2017).
28. Juergens, N. Exploring common ground for different hypotheses on Namib fairy circles. *Ecography* **38,** 001–003 (2015).
29. Thorne, B. L. & Haverty, M. I. A review of intracolony, intraspecific, and interspecific agonism in termites. *Sociobiology* **19,** 115–145 (1991).
30. Liu, Q.-X. *et al.* Pattern formation at multiple spatial scales drives the resilience of mussel bed ecosystems. *Nature Commun.* **5,** 5234 (2014).

Supplementary Information is linked to the online version of the paper at www.nature.com/nature.

Acknowledgments: This research is a product of U.S. National Science Foundation grant DEB-1355122 to C.E.T. and R.M.P. J.A.B. was supported by the Marine Alliance for Science and Technology for Scotland (MASTS) pooling initiative, funded by the Scottish Funding Council (HR09011) and contributing institutions. WorldView-2 satellite imagery was obtained through a grant from the DigitalGlobe Foundation to R.A.L. We thank: the Government of Namibia and the NamibRand Nature Reserve for permission to conduct research; A. Lamb, D. Doak, G. Barrenechea, P. Davies, S. Levin, R. Martinez-Garcia, I. Rodriguez-Iturbe, A. Sabatino, J. Ware for helpful discussions; I. Arndt for Australian termite-mound images used in analysis and shown in ED Fig. 3; and F. Lanting for connecting us to NamibRand and for use of the image in Fig. 3d.

Author contributions: C.E.T., J.A.B., and R.M.P. conceived the study and developed the models, with input from E.S. J.A.B performed point-pattern analyses and all simulations. E.S. performed Voronoi and Fourier Transform analyses. J.A.G., T.C.C., and R.A.L. contributed field data and remote-sensing analyses. C.E.T., J.A.B., and R.M.P. drafted the paper, and all authors provided comments.

Author information: Data are available on Dryad. Reprints and permissions information is available at www.nature.com/reprints. The authors declare no competing financial interests. Correspondence and requests for materials should be addressed to ctarnita@princeton.edu and juan.bonachela@strath.ac.uk

Fig. 1. **Social-insect nest distributions, in theory and in nature. a.** Model results: dots = centers of mature nest sites; parameterization in Extended Data Table 1. See Supplementary Video 1 for model dynamics. **b-e.** Remotely sensed images of hexagonal termite and ant nests in (b) Kenya (false-color composite Quickbird satellite image, red circles indicate *Odontotermes montanus* mound locations); (c) Brazil (*Syntermes dirus*; GoogleEarth); (d) Arizona, USA (*Pogonmyrmex barbatus*; GoogleEarth); (e) Mozambique (*Macrotermes* sp.). Features shown in (b–e) have been ground-truthed as social-insect nests (see Methods and Supplementary Text 4.1). **f.** Fairy circles (FCs) in Namibia (GoogleEarth). **g.** Neighbor-number distributions from Voronoi-diagram analysis; bars left-to-right correspond to legend top-to-bottom. **h-i.** Pair correlation and Ripley's *L* functions (red curves) for model results (top), Kenya (middle), and FCs (bottom). Shaded areas represent 95% simulation envelopes to discern from complete spatial randomness. Details of images and analyses in Methods and Supplementary Information.

Fig. 2. Simulation of FC emergence from termite engineering and vegetation feedbacks. a. Termite nest (blue dot) with circular foraging territory. **b-c.** Characteristic FC vegetation arising around nest site after (b) dry and (c) wet seasons; brown = soil; green = vegetation; darker green indicates greater biomass according to color gradient bar (units = kg/m^2). **d-f.** Predicted soil-moisture, root-density, and plant-density profiles along 30-m transects through FCs (0 = nest center). Parameterization in Extended Data Tables 1 and 2.

Fig. 3. FC life cycle in the coupled termite-vegetation model. a. Nest centers and foraging territories [blue dots = mature colonies; red dots = incipient nests (including the initial diggings of an alate pair)]. **b-c.** FCs and matrix vegetation following (b) dry and (c) wet seasons; color scheme per Fig. 2b. **d.** Oblique aerial photo of FCs at NamibRand (image courtesy of Frans Lanting). **e-p.** Termite-colony dynamics (e-j) and, below each panel, corresponding FC vegetation dynamics (k-p). Red arrow in k-p indicates location of FC shrinkage and disappearance following colony death (red arrow in e). Blue arrow in n-p indicates location of FC appearance and growth following colony establishment (blue arrow in h-j). See Supplementary Video 2 for model dynamics. Parameterization in Extended Data Tables 1 and 2.

Fig. 4. Predicted and observed regular patterning of FC matrix vegetation. a. Panorama of NamibRand FC landscape showing matrix-vegetation clumps. **b.** Low-altitude (10-m) photograph of matrix vegetation. Scale bar same as in panel c. **c.** Model output used for comparison with b. Parameterization in Extended Data Tables 1 and 2. **d.** Normalized radial spectra of field images (n=27 samples) and model simulations (n=52 samples), as functions of wavenumber. See dynamics of matrix vegetation in Supplementary Video 3.

Methods.

Termite dynamics. To characterize the emergent spatial organization of termite nests, we developed a general mechanistic model for termite colony growth, reproduction, foraging behavior, and intraspecific competition (see complete description in the Supplementary Information). For computational convenience, we update these dynamics on a yearly basis. We consider a finite landscape consisting of a regular square lattice. As the initial condition, a single colony founds a nest at a random location within the grid, with a starting population of 2 termites (queen and king) and a minimum viable foraging area $A_{\min}$. This inaugural colony grows, reproduces, and seeds the rest of the system with new incipient colonies; the system develops with time according to the rules detailed below. Each colony, i, is characterized by its population biomass, $B_i(t)$, and total foraging-territory area, $A_i(t)$.

Foraging territory area: Termites forage outward from the nest, which is situated at the center of the initial territory. Thus territories expand in a circular fashion; however, because expansion in certain directions may be blocked by other colonies (see *Competition*), territory shape does not necessarily remain circular or centered on the nest proper. $R_i(t)$ denotes the largest radial distance within the territory, measured from the center of the nest; this radius is constrained physiologically by R_{max}, the maximum distance that a foraging termite can travel.

Nest: We assume that the physical nest proper occupies a circular area, $M_i(t)$ (centered at the center of the initial territory), whose radius is a fraction of $R_i(t)$ given by f_m.

Colony growth: We model colony size and growth in terms of biomass and, consistent with empirical data[31], we assume that termite colonies grow logistically. Production of new colony members, μ, is determined by the queen's constant rate of egg-laying. The carrying capacity, $B_{\max}$, represents the maximum possible biomass that a colony can reach, a limit that we assume to be imposed by intrinsic physiological constraints (e.g., how big a nest structure the colony can construct) and thus equivalent for all colonies. Colony members die at a per capita mortality rate m. The effective carrying capacity is therefore $B_{\max}(1-m/\mu)$. To meet basic energetic maintenance costs and achieve growth, colonies require resources. Specifically, the resources needed to maintain colony i at size $B_i(t)$ are given by: $\rho_i^{\text{need}} = B_i(t)/c$, where c is the termite assimilation capacity (i.e., the conversion factor from resource biomass into termite biomass). This resource requirement is to be compared with the resources available in the foraging territory. Since we model termites that feed exclusively on dead plant material, we assume that resource availability for colony i at time t at any given location x within that colony's territory is equal to the amount of dead plant material that has accumulated at that location during the previous year. Assuming that plant mortality occurs at a constant rate, m_P, and given that colony i occupies area $A_i(t)$ at time t, the resources available to colony i, $\rho_i(t)$, are:

$$\rho_i(t) = \int_{A_i(t)} \int_{1 \text{ year}} m_P P(\vec{x}, t') dt' d\vec{x}$$

where $P(x, t)$ is the live plant biomass at location x and time t. This will be obtained from the dynamics of the vegetation model below. Because termite dynamics are updated annually, resource requirement and availability are compared at the beginning of each year. If $\rho_i \neq \rho_i^{\text{need}}$, the colony will try to adjust its foraging territory accordingly: if resources are insufficient ($\rho_i < \rho_i^{\text{need}}$), the colony will expand its foraging territory trying to obtain the necessary resources; conversely, if resources are in excess ($\rho_i > \rho_i^{\text{need}}$), termites will not need to travel as far to harvest the minimum necessary resources, and the foraging territory will shrink. Such shrinkage produces "empty" (unoccupied) area potentially available for nearby colonies as additional

foraging territory. If territory expansion is hindered for any reason (e.g., lack of available space, or R_{max} being reached), then colony biomass will grow only as much as allowed by the resources available up to the point of hindrance.

Territorial competition: If territory expansion leads to overlap with the territory of another colony, we assume that a conflict ensues at the border between the two territories in the form of direct interference competition, avoidance, and/or aggressive territorial defense (such antagonism between intraspecific colonies is common among many, perhaps most, species of termites and ants[29,32]). These conflicts can simply remain as border skirmishes (i.e., offsetting mortalities, neither colony gains any net ground) or can lead to "wars" that may result in the extermination of one colony. We assume that smaller, growing colonies exhibit more aggressively expansionist tendencies than do larger established ones, in keeping with evidence that aggression declines with distance from the nest[33] (Fig. S1A). The outcome is probabilistic, with Pr (i and j at war) = Pr (i seeks war) × Pr (j seeks war), where:

$$\Pr(i \text{ seeks war}) = \frac{1}{1 + e^{-\beta_2(1-\alpha_2 S_i(t))}}, \qquad \text{with} \qquad S_i(t) = \frac{B_i(t)}{B_{\max}}$$

War results either in the death of one colony (highly probable if there is a substantial size discrepancy since we assume ~1:1 mortality in conflict) or in coexistence (if sizes are similar), in which case the workers' foraging radius is truncated, a boundary is established, and expansion ceases in that direction. If colonies i and j fight, then i wins with probability:

$$\Pr(i \text{ beats } j) = \frac{1}{1 + e^{-\beta(1-\alpha S_j(t)/S_i(t)}}$$

If colony i dies in conflict, the winning colony j also suffers losses in the form of reductions in both territory and population biomass: $A_j' = A_j - A_i$, and B_j is reduced proportionally [i.e. $B_j' = B_j (A_j'/A_j)$]. In the rare event that the winning colony has a smaller territory and biomass than the losing one, then both territory and population biomass are decreased to a fraction q of the original: $A_j' = qA_j$. In either case, the winning area cannot be reduced below the minimum, $A_{\min}$.

Reproduction: We assume that when colonies reach a certain population biomass, $B_{\text{mat}} < B_{\max}$, they become reproductively mature (a.k.a. established) and produce alates (winged dispersing future queens and kings) as follows. If, during the current time step, colony i shrinks in biomass due to resource limitation, then it forgoes reproduction even if its newly reduced biomass exceeds B_{mat}; otherwise, it produces a number of alates proportional to a fraction f_A of its biomass. In our simulations we assume that these alates disperse randomly and in pairs over the entire grid. If an alate pair lands within the territory of an established colony or does not have enough space to initiate (i.e., available area at the landing point < A_{min}), the alates die. Otherwise, they start a new colony. The landing point is assumed to be the center of the new nest.

Mortality: There are two sources of mortality for colonies. The first is conflict between neighbors (see above), which we assume to be the primary cause of death in small colonies, but to decline in importance as colonies grow. Indeed, empirical observations from multiple systems suggest that territorial conflict eliminates many incipient colonies but seldom leads to the death of a mature colony, whereas mature colonies show signs of perpetual conflict at outer edges of their foraging territories[34-36]. The second source of mortality is an intrinsic stochastic death rate, which primarily affects established colonies. We let m_C be stochastic mortality for large colonies and set it to replicate a realistic lifetime for mature colonies[31,37].

Termite engineering: Here, we focus on the scenario in which termites locally deplete plant biomass, as hypothesized for the sand termite *Psammotermes allocerus* (Rhinotermitidae), which has been suggested as the cause of the Namib FCs[7]. On nests, we assume the mortality

rate of plant biomass to be elevated by a fixed proportion ν: $m_{P\,\mathrm{off}} = m_P;\ \ m_{P\,\mathrm{on}} = \nu\, m_{P\,\mathrm{off}}$. For full model details and analysis see SI; for parameterization see Extended Data Table 1.

Vegetation dynamics. To model vegetation dynamics, we modified a model that has been used repeatedly to describe and reproduce the patterns of self-organization that are typical of vegetation in semi-arid environments[15]. The model considers the dynamics of vegetation (*P*), soil water (*W*), and surface water (*O*) densities. Assuming a flat terrain, the model can be written as:

$$\frac{\partial P(\vec{x},t)}{\partial t} = G_P(\vec{x},t)P(\vec{x},t)\left(1-\frac{P(\vec{x},t)}{K}\right) - m_P P(\vec{x},t) + D_P\nabla^2 P(\vec{x},t) \quad (1)$$

$$\frac{\partial W(\vec{x},t)}{\partial t} = \gamma\frac{P(\vec{x},t)+QW_0}{P(\vec{x},t)+Q}O(\vec{x},t) - N\left(1-\frac{R_{educ}P(\vec{x},t)}{K}\right)W(\vec{x},t) - G_W(\vec{x},t)W(\vec{x},t) + D_W\nabla^2 W(\vec{x},t) \quad (2)$$

$$\frac{\partial O(\vec{x},t)}{\partial t} = R_{ainfall} - \gamma\frac{P(\vec{x},t)+QW_0}{P(\vec{x},t)+Q}O(\vec{x},t) + D_O\nabla^2(O^2(\vec{x},t)) \quad (3)$$

where ∇^2 represents the nabla operator (second spatial derivative) and the values and meaning of parameters can be found in Extended Data Table 2. The first term in Eq.(3) represents rainfall, the second term represents infiltration of surface water into the soil, and the third term represents water (superficial) diffusion. The first term in Eq.(2) represents the increase in soil water due to infiltration, whereas the second term represents evaporation, the third term represents soil water uptake, and the last term soil water diffusion. Lastly, the first term in Eq.(1) represents plant growth due to water uptake, the second term represents mortality, and the third term vegetation biomass diffusion (via e.g. seed dispersal). In turn, G_P and G_W, plant growth rate and soil water consumption rate respectively, depend on the extension of the root system. Thus, if the root system is encoded in the kernel:

$$G(\vec{x},\vec{x}',t) = \frac{1}{2\pi S_0^2}\exp\left[-\frac{|\vec{x}-\vec{x}\prime|^2}{2\left[S_0\left(1+EP(\vec{x},t)\right)\right]^2}\right] \quad (4)$$

the effect of roots on growth and water consumption, respectively, is given by:

$$G_P(\vec{x},t) = \Lambda\int_L G(\vec{x},\vec{x}',t)W(\vec{x}',t)d\vec{x}'$$

$$G_W(\vec{x},t) = \Gamma\int_L G(\vec{x}',\vec{x},t)P(\vec{x}',t)d\vec{x}'$$

where the integrals consider the totality of the system[38]. The kernel determines to what extent roots from a body of vegetation biomass (e.g. clump) can use water and influence other parts of the system. Specifically, the Gaussian kernel above sets this distance through its standard deviation, the root-system size, given by $S_0\left(1+EP(\vec{x},t)\right)$.

Variable rainfall: We used data to replace the constant average rainfall (typically used in models such as the one above) by a more realistic variable rainfall function $R_{ainfall}(t)$ that captures the typical Namib yearly rainfall. To that end, we used data from 2004-2014 from multiple Namib desert locations (provided by Vanessa Hartung) to calculate mean monthly rainfall in a "average" year along with standard errors reflecting among-year variation in monthly totals. The resulting $R_{ainfall}(t)$ depicts the two distinct seasons (wet and dry) characteristic of this region (see Extended Data Fig. 5):

$$R_{ainfall}(t) = R_0 10^{\omega\sin\left(\frac{(t+1)\pi}{6}\right)}[1+\sigma_R\eta(t)] \quad (5)$$

Here, *t* is the month of the year, and the second term in brackets represents noise (random number uniformly distributed between *0* and σ_R) that takes into account an additional source of stochasticity inherently associated with the weather.

Asymmetric roots: One important feature of the vegetation model above is that the root system represented by the Gaussian kernel, Eq. (4), is symmetric and therefore root density is equivalent in all directions, regardless of heterogeneities in water availability. However, desert-plant roots in sandy substrates both (a) grow preferentially in the direction of localized moisture concentrations (hydrotropism) and (b) exhibit enhanced proliferation, branching, and biomass growth in moist vs. dry soil, breaking the symmetry of root architecture in ways thought to enable "precise exploitation of water patches and drought avoidance)[39]. We therefore modified the above model to incorporate the possibility of hydrotropism and asymmetric root proliferation (or asymmetric exploitation of soil moisture) in response to localized differences in soil-water availability. Once the soil-moisture difference dissipates, the root system in that direction returns to its original growth pattern. We introduced an additional term in the plant-growth equation, Eq.(1), that modifies plant growth rate by a specific factor. This is calculated by adding to the existing term $G_P(x,t)$, an additional contribution from any direction in which soil water surpasses a site-specific threshold, W_{th}: $\tilde{G}_P(\vec{x},t) = G_P(\vec{x},t)[1 + \omega' F_{\text{asym}}(\vec{x},t)]$, where ω' is a (dimensionless) diminishing factor (in our simulations, $\omega' = 0.5$), necessary to prevent numerical instabilities leading to unrealistic features such as system-wide plant clusters, and F_{asym} is the improvement function *per se*, given by:

$$F_{\text{asym}}(\vec{x},t) = \langle W(\vec{x}',t)/W(\vec{x},t)\rangle_{\vec{x}'} \quad (6)$$

The <…> symbol represents spatial averages as follows: following Eq. (4), the standard deviation of the Gaussian root system is given by $S_0\big(1 + EP(\vec{x},t)\big)$; therefore, a rough estimate of the maximum length of the root system is given by three times that standard deviation. Thus, the spatial averages in Eq. (6) consider locations at a distance $|\vec{x} - \vec{x}'| \approx 3S_0(1 + EP(\vec{x},t))$ and use the immediate neighborhood of these locations to assess the average water availability and how different it is from $W(\vec{x},t)$. Because our simulations occur on a square lattice, such spatial average only considers the 4 neighbors of a location $\vec{x}'$. However, only nearest neighbors of $\vec{x}'$ fulfilling:

$$\frac{W(\vec{x}'_{nn},t)}{W(\vec{x},t)} - W_{thr} > 0$$

are considered for the average, which ensures that only a sufficiently large contrast between the focal location *x* and the neighborhood of $\vec{x}'$ triggers this differential root growth. In our simulations, we set W_{th}=4.

Parameterization and sensitivity analysis. We thoroughly searched the existing literature to identify plausible (and internally consistent) values of individual-, colony-, and population-level parameters such as termite individual biomass, thresholds for maturity and reproduction, as well as the parameters related to the vegetation model (Extended Data Tables 1 and 2). For the latter, we modified prior parameterizations[15] to tailor the model to Namib-desert conditions (e.g., the variable rainfall function described above, low surface-water diffusivity). In addition, we conducted sensitivity analyses to test the dependence of the model outputs on each of the different parameters. Finally, because we used a spatial discretization to enhance the speed of our simulations, we conducted additional sensitivity analyses to test the appropriateness of (i) the spatial grain and (ii) topology (square vs. hexagonal lattice) of the underlying grid, showing that these assumptions did not affect the results.

Insect-nest distributions: field data. We used high-resolution satellite imagery to quantitatively analyze the spatial distribution of social-insect nests in four countries on three continents: termite

mounds in Kenya (Macrotermitinae: *Odontotermes montanus*; Fig. 1b), Mozambique (Macrotermitinae: *Macrotermes* spp.; Fig. 1e), Brazil (Termitidae: *Syntermes dirus*; Fig. 1c), and Australia (Termitidae: *Amitermes meridionalis*), along with harvester ant nests in the southwestern USA (Formicidae: *Pogonomyrmex* spp.; Fig. 1d). We further re-analyzed the Namibian FC sites of a prior study[10] to ensure concordance and comparability with our other analyses. In all cases, these features were clearly distinguishable in imagery (Fig. 1, Extended Data Fig. 3) and the identities of the insect species that built them have been unambiguously established in published field studies (Supplementary Text 4.1). The regions and locations analyzed are as follows:

Kenya—Two topographically, edaphically, and floristically homogeneous rectangular areas (0.975 km^2 and 1.201 km^2, comprising 205 and 241 mounds, respectively) in clay-rich vertisols at Mpala Research Centre (~0°17' N, 36°51' E), where our prior work has extensively ground-truthed mound locations[3], from multispectral QuickBird satellite imagery.

Mozambique—A subsection of a 0.630-km^2 rectangular area of mixed *Acacia*/palm savanna-woodland in Gorongosa National Park (~18°57' S, 34°21' E) comprising ~152 total mounds, from multispectral WorldView-2 satellite imagery; this analysis was comprehensively ground-truthed by mapping all mounds on foot.

Brazil—Two areas (0.209 and 0.409 km^2, comprising ~452 and 751 mounds, respectively), in Bahia State (~12°30' S, 41°37' W), from Google Earth.

North America—Two areas of 0.308 and 0.179 km^2, comprising ~510 and 224 nests, respectively, in Arizona (~36°15' N, 113°05' W), from Google Earth.

Namibia—Three Namib-Desert sites within the Giribes Plain (G) and Marienfluss Valley (MV), within the same rectangular areas analyzed in prior work[10], with aerial extents of 0.288 (G1), 0.294 (G2), and 0.322 km^2 (MV), and comprising 1181, 1288 and 676 FCs, respectively, from Google Earth.

Australia—Two oblique aerial photographs (courtesy of photographer Ingo Arndt) of *Amitermes* mounds in Litchfield National Park, comprising 249 and 295 mounds, respectively. Specific geographic coordinates for these images are unknown, and we were unable to analyze these mounds in satellite images; generic coordinates for Litchfield are ~13°17' S, 130°45' E.

Insect-nest distributions: quantitative analysis. We analyzed the spatial distribution of termite mounds, ant nests, and fairy circles (henceforth, "points"). We computed Voronoi tessellations[10,40] for the point patterns, from which we extracted the following information: (1) distributions of nearest-neighbor numbers for each point, i.e., the number of corners of each Voronoi tile, which provides information on the regularity of the pattern (Fig. 1g, Extended Data Fig. 3); (2) distributions of tile areas (mean area and coefficient of variation); and (3) distributions of the distances of all points to their nearest neighbor[10]. We further calculated pairwise correlation (PCF) and Ripley's *L* functions[41] for each different area (see Supplementary Information and Extended Data Fig. 4). We used both the "spatstat" package[41] in R and our own Fortran code to calculate both functions. We also used R's "spatstat" for the calculation of significance envelopes. We used the same approach to analyze the output of the theoretical model (Fig. 1g, Extended Data Figs. 2,3,4).

Vegetation patterns: field data. We collected low-altitude aerial imagery of Namibian FC and matrix vegetation at the Namib Rand Nature Reserve (NRNR) in southern Namibia (25.04º E, 15.94º S), where fairy circles have been intensively studied and biotic/abiotic conditions are well

characterized[6,7,12]. Mean annual precipitation is 70-80 mm[6], falling mostly from December-May. The site consists of Kalahari sand plains and dunes typical of the habitat in which Fairy Circles are found[6,7,12]. The flora is co-dominated by three congeneric bushman-grasses: *Stipagrostis obtusa*, *S. uniplumis*, and *S. ciliata*[12]. In February 2015, we selected 10 sites spanning ~35km within NRNR. At each site, we haphazardly selected 10 pairs of fairy circles and measured the distance between circles (from one outer ring edge to another) and the size of each FC (average of two perpendicular diameters within the vegetation ring). The mean (± SEM) diameter of FCs in our dataset was 5.94 ± 0.23 m, and the mean distance between circles was 6.9 ± 0.4 m. Low-altitude imagery was collected at a subset of three sites: the most northern (24.94º E, 25.95º S), the most southern (25.25º E, 16.02º S), and the most central (25.13º E, 16.01º S). We photographed matrix vegetation at the midpoint between 30 pairs of neighboring FCs (n = 10 pairs per site; Fig. 4b) using a digital camera (Canon PowerShot S110), mounted on an 11-m carbon-fiber pole (Ron Thompson Gangster Carp Pole) such that it could be held parallel to the ground at 10-m height. Prior to imaging, we manually removed fallen leaf litter that might have obscured spatial patterns in standing vegetation. Exposure was controlled manually to maintain consistency in changing light conditions. For all images, this camera rig was held at constant height by the same individual (TCC). A reference object was placed in all images and used to scale them to a pixel size of 0.333 cm.

Vegetation patterns: quantitative analysis. Images were scaled and a large rectangular sub-area of similar size (1340 × 1340 pixels for two sites, and 900 × 900 pixels for a site in which fairy circle density was higher) was selected from each image to comprise only grass and soil (i.e., no fairy circles) and no visible disturbance (n=27 images; three of the images were excluded because they did not have a large enough area between circles). Images were processed as in[4]. For comparison with the model simulations with stochastic seasonal rainfall, we selected snapshots of the simulated vegetation in the wet season in different years (we used snapshots from February, corresponding to when the field images were collected in 2015). From these snapshots, we selected 2 subsections (73 × 73 and 135 × 135 pixels) between neighboring FCs (n = 52, 26 years × 2 subsections year^{-1}). We transformed the patterns of biomass density from the model into binary images (vegetation vs. bare soil; see Fig. 4c) according to a lower threshold found from temporal and spatial analyses of the model data (0.015 Kg/m^2). We used the two-dimensional (2D) Fourier transform and a subsequent computation of the 2D periodogram (i.e., power spectrum[42]), to provide a quantitative characterization of the spatial patterns[43]. We then calculated the radial spectrum $\boldsymbol{r}$ (sum of the periodogram values on concentric ring-shaped regions of the 2D surface), to quantify the portion of image variances that can be accounted for by a simple cosine wave repeating itself r times (wavenumber) along a travel direction of the periodogram. We normalized the radial spectra for: (a) wavenumber, by dividing $\boldsymbol{r}$ by the size of the domain in the analyzed image (ca. 4.45 and 3 m for field images and 3.65 to 6.75 m for simulations); and (b) amplitude of the radial spectrum, by dividing by the maximum of the mean.

31. Collins, N. M. Populations, age structure and survivorship of colonies of *Macrotermes bellicosus* (Isoptera: Macrotermitinae). *J. Anim. Ecol.* **50,** 293–311 (1981).
32. Holldobler, B. Territoriality in ants. *Proc. Amer. Phil. Soc.* **123,** 211–218 (1979).
33. Adams, E. S. Territory size and shape in fire ants: a model based on neighborhood interactions. *Ecology* **79,** 1125–1134 (1998).
34. Darlington, J. P. The underground passages and storage pits used in foraging by a nest of

the termite *Macrotermes michaelseni* in Kajiado, Kenya. *J. Zool.* **198,** 237–247 (1982).
35. Palmer, T. M. Wars of attrition: colony size determines competitive outcomes in a guild of African acacia ants. *Anim. Behav.* **68,** 993–1004 (2004).
36. Abe, T., Bignell, D. E. & Higashi, M. *Termites: Evolution, Sociality, Symbioses, Ecology*. (Springer, 2000).
37. Keller, L. Queen lifespan and colony characteristics in ants and termites. *Insect. Soc.* **45,** 235–246 (1998).
38. Gilad, E. & von Hardenberg, J. A fast algorithm for convolution integrals with space and time variant kernels. *J. Comput. Phys.* **216,** 326–336 (2006).
39. Guevara, A. & Giordano, C. V. Hydrotropism in lateral but not in pivotal roots of desert plant species under simulated natural conditions. *Plant and Soil* **389,** 257–272 (2014).
40. Illian, J., Penttinen, A., Stoyan, H. & Stoyan, D. *Statistical Analysis and Modelling of Spatial Point Patterns*. (John Wiley & Sons, Ltd, Chichester, UK, 2008).
41. Baddeley, A., Rubak, E. & Turner, R. *Spatial Point Patterns: Methodology and Applications with R*. (Chapman and Hall/CRC, 2015).
42. Mugglestone, M. A. & Renshaw, E. Detection of geological lineation on aerial photographs using two-dimensional spectral analysis. *Comput. Geosci.* **24,** 771–784 (1998).
43. Couteron, P. & Lejeune, O. Periodic spotted patterns in semi-arid vegetation explained by a propagation-inhibition model. *J. Ecol.* **89,** 616–628 (2001).
44. Tschinkel, W. R. The foraging tunnel system of the Namibian desert termite, Baucaliotermes hainesi. *J. Insect Sci.* **10,** 65 (2010).
45. Baker, P. B. & Haverty, M. I. Foraging populations and distances of the desert subterranean termite, *Heterotermes aureus* (Isoptera: Rhinotermitidae), associated with structures in southern Arizona. *J. Econ. Entom.* **100,** 1381–1390 (2007).
46. Jones, S. C. Colony size of the desert subterranean termite *Heterotermes aureus* (Isoptera: Rhinotermitidae). *Southwest. Nat.* **35,** 285–291 (1990).
47. Haagsma, K. A. & Rust, M. K. Colony size estimates, foraging trends, and physiological characteristics of the western subterranean termite (Isoptera: Rhinotermitidae). *Environ. Entomol.* **24,** 1520–1528 (1995).
48. Grace, J. K., Abdallay, A. & Farr, K. R. Eastern subterranean termite (Isoptera: Rhinotermitidae) foraging territories and populations in Toronto. *Canad. Entomol*. **121,** 551–556 (1989).
49. Husseneder, C., Powell, J. E., Grace, J. K., Vargo, E. L. & Matsuura, K. Worker size in the Formosan subterranean termite in relation to colony breeding structure as inferred from molecular markers. *Environ. Entomol.* **37,** 400–408 (2008).
50. Wood, T. G. & Sands, W. A. The role of termites in ecosystems. In *Production Ecology of Ants and Termites* (ed. Brian, M. V.) pp. 245–292 (Cambridge Univ. Press, 1978).
51. Matsuura, K. Colony-level stabilization of soldier head width for head-plug defense in the termite *Reticulitermes speratus* (Isoptera: Rhinotermitidae). *Behav. Ecol. Sociobiol*. **51,** 172–179 (2002).
52. Darlington, J. P. E. C. Turnover in the populations within mature nests of the termite *Macrotermes michaelseni* in Kenya. *Insect. Soc.* **38,** 251–262 (1991).
53. Hadley, N. F. & Szarek, S. R. Productivity of desert ecosystems. *BioScience* **31,** 747–753 (1981).
54. Thorne, B. L., Breisch, N. L. & Muscedere, M. L. Evolution of eusociality and the soldier

caste in termites: influence of intraspecific competition and accelerated inheritance. *Proc. Natl. Acad. Sci. USA* **100,** 12808–12813 (2003).
55. Golodets, C. *et al.* Climate change scenarios of herbaceous production along an aridity gradient: vulnerability increases with aridity. *Oecologia* **177,** 971–979 (2015).
56. Cain, M. L. & Damman, H. Clonal growth and ramet performance in the woodland herb, *Asarum canadense*. *J. Ecol.* **85,** 883–897 (1997).
57. Milton, S. J. & Dean, W. Disturbance, drought and dynamics of desert dune grassland, South Africa. *Plant Ecol.* **150,** 37–51 (2000).
58. Evangelides, C., Arampatzis, G. & Tzimopoulos, C. Estimation of Soil Moisture Profile and Diffusivity Using Simple Laboratory Procedures. *Soil Sci.* **175,** 118–127 (2010).
59. Danin, A. *Plants of Desert Dunes* (Springer Science & Business Media, 2012).
60. Sheffer, E., Yizhaq, H., Shachak, M. & Meron, E. Mechanisms of vegetation-ring formation in water-limited systems. *J. Theor. Biol.* **273,** 138–146 (2011).

Data availability statement. The datasets generated and analysed during the current study are available in the Dryad repository. The computer code is available from the corresponding authors upon request.

Extended Data Figure Legends

Extended Data Figure 1. Probability functions associated with conflicts in the termite model. a. probability for colony *i* and colony *j* to engage in a war as a function of each colony's population biomass. **b.** If colonies *i* and *j* engage in a war, probability function for colony *j* to win the war as a function of the ratio of colony population biomass.

Extended Data Figure 2. Results of the termite self-organization model with a fixed resource density level, P_{cst}. a-b. Temporal behavior of *mature* colonies in the termite model for $P_{cst} = 50$ g/m^2. **a.** Average diameter of mature nests (blue shading represents ± 1 SD). **b.** Average distance between nearest neighbors, (where neighbors are nests that share territory borders). Both observables reach a clear stationary state after a transient period of ~200 years. **c-f.** Emergent behavior for the colonies at the stationary state as a function of the (annually) available level of resources. **c.** Average mound diameter, which reflects foraging-territory area, decreases as resource availability increases. **d.** Mean nearest-neighbor distance also decreases with increasing resource density. **e.** Termite population density (# of individuals/m^2) increases with available resources. **f.** Average colony biomass density (individuals/colony) increases with available resource density, and reaches a saturation value around $B_{\max}(1-m/\mu)$ (see Supplementary Information). **g.** Frequency distribution of neighbor numbers from Voronoi analysis for the model with different resource densities (inset: mean number of neighbors). Higher resource densities result in a higher number of colonies (numbers in parentheses in the legend) and therefore more powerful results. Results are obtained by averaging over 100 simulations for each resource level; error bars show ± 1 SD.

Extended Data Figure 3. Average number of neighbors in various field locations. Upper left panel: Average number of neighbors (± 1 SD) from Voronoi analysis of model and field data; number of nests at each location is shown in parentheses. **All other panels:** Satellite imagery and/or photographs used for data analysis. Mounds are highlighted for ease of observation. If a white rectangle is present then only the points within the rectangle were analyzed; otherwise, the whole image was analyzed. Scale bars = 100m. (Aerial imagery of *Amitermes* mounds in Australia courtesy of Ingo Arndt. Satellite imagery: Kenya (QuickBird); Mozambique (WorldView-2); all others are from Google Earth.

Extended Data Figure 4. Spatial point-pattern analyses of various field locations. Left: Pair correlation function as a function of distances between nests. **Right:** Ripley's *L* function for the same examples. 95% pointwise simulation envelopes (shaded areas) were calculated using the default function from the R package spatstat. These envelopes allow us to reject the null hypothesis (complete spatial randomness) at a confidence level of 95%; thus, if the focal function (red line) falls out of the envelope for a given distance r, the function differs from the expectation for a completely-random point distribution. Both sets of panels show peaks (left panels) or valleys (right panels) of regularity that indicate the presence of overdispersion for each of these examples. Note the different number of nests present in the samples from each location (Extended Data Figure 3), which leads to different levels of noise in the calculation of the two statistics.

Extended Data Figure 5. Rainfall data from NamibRand. Top: 10-year time-series of monthly rainfall totals 2004-2014, averaged across multiple sites within NamibRand Nature Reserve (data provided by Vanessa Hartung). **Bottom:** Mean monthly rainfall (i.e., averaged for each month across all years) in NamibRand from 2004-2014 (green line, ± 1SD in red) and proposed rainfall function (blue). The noise term included in $R_{ainfall}(t)$ [Eq.(5) in Methods] ensures that the rainfall function variability is high during the rainy season and low in the dry season, consistent with the data.

Extended Data Figure 6. Vegetation dynamics with and without termite engineering. a-b. Comparison of the stationary pattern obtained with the vegetation model alone using **a.** the original symmetric implementation for the root kernel and **b**. the modified root kernel that is allowed to grow asymmetrically; **c-d.** Stationary pattern obtained with the naïve setup (i.e. one single, static colony in the center of the system; constant rainfall); **c.** the resulting pattern using the original, symmetric root kernel; **d.** the pattern obtained when the asymmetric root system growth is implemented; **e-f.** Simulation run measuring the recovery time after the death of a colony in the coupled model with variable rainfall and asymmetric roots. **e.** System a few months before reaching stationarity; a ring of taller and denser vegetation is formed around the gap, and matrix vegetation is reaching its stationary clumpy distribution. **f.** Several decades after colony death, the gap closes fully, and the remaining large matrix clumps disappear shortly thereafter. Brown = soil; green = vegetation. Color intensity indicates vegetation density. Parameters are as in Extended Data Tables 1 and 2.

Extended Data Figure 7. The effect of decreasing termite-induced plant mortality or increasing rainfall in the coupled system. When on-nest enhanced plant mortality is low and/or

rainfall is high, vegetation growth outpaces termite engineering and, consequently vegetation is found also on nests, disrupting (and for high enough rainfall values completely removing) the bare discs. **a.** Low mortality enhancement ($\nu = 1.1$); **b.** Intermediate mortality enhancement ($\nu = 1.25$); values in (a-b) are both lower than in Extended Data Table 1 but have same average rainfall as Extended Data Fig.5; **c.** Intermediate mortality enhancement ($\nu = 1.25$) and average rainfall increased by 10%. Brown = soil; green = vegetation. Color intensity indicates vegetation density. **d-f.** Corresponding underlying termite territories and nests. Blue dots = established nests; red dots = incipient nests (including the initial diggings of an alate pair, leading to occasionally high local densities as shown in **f**). Snapshots taken for a peak in vegetation after the system has reached stationarity. Rest of the parameters as in Extended Data Tables 1 and 2.

Extended Data Figure 8. Distribution of FC lifetimes measured in the coupled model. For $n = 9$ replicates of the merged model, we kept track for ~300 years (until the end of the simulation) of 100 randomly selected FCs that were born after the stationary state (reached after ~100 years). 53 of these FCs disappeared before the end of the simulation, allowing lifespan estimates for that subset. The resulting lifespans range from <5 years to >165 years, within reported estimates for Namib FCs. Note that the distribution is truncated on the right tail due to the limit of available simulation times; however, the overall shape of the distribution should not be strongly affected since such long-lasting FCs are very infrequent.

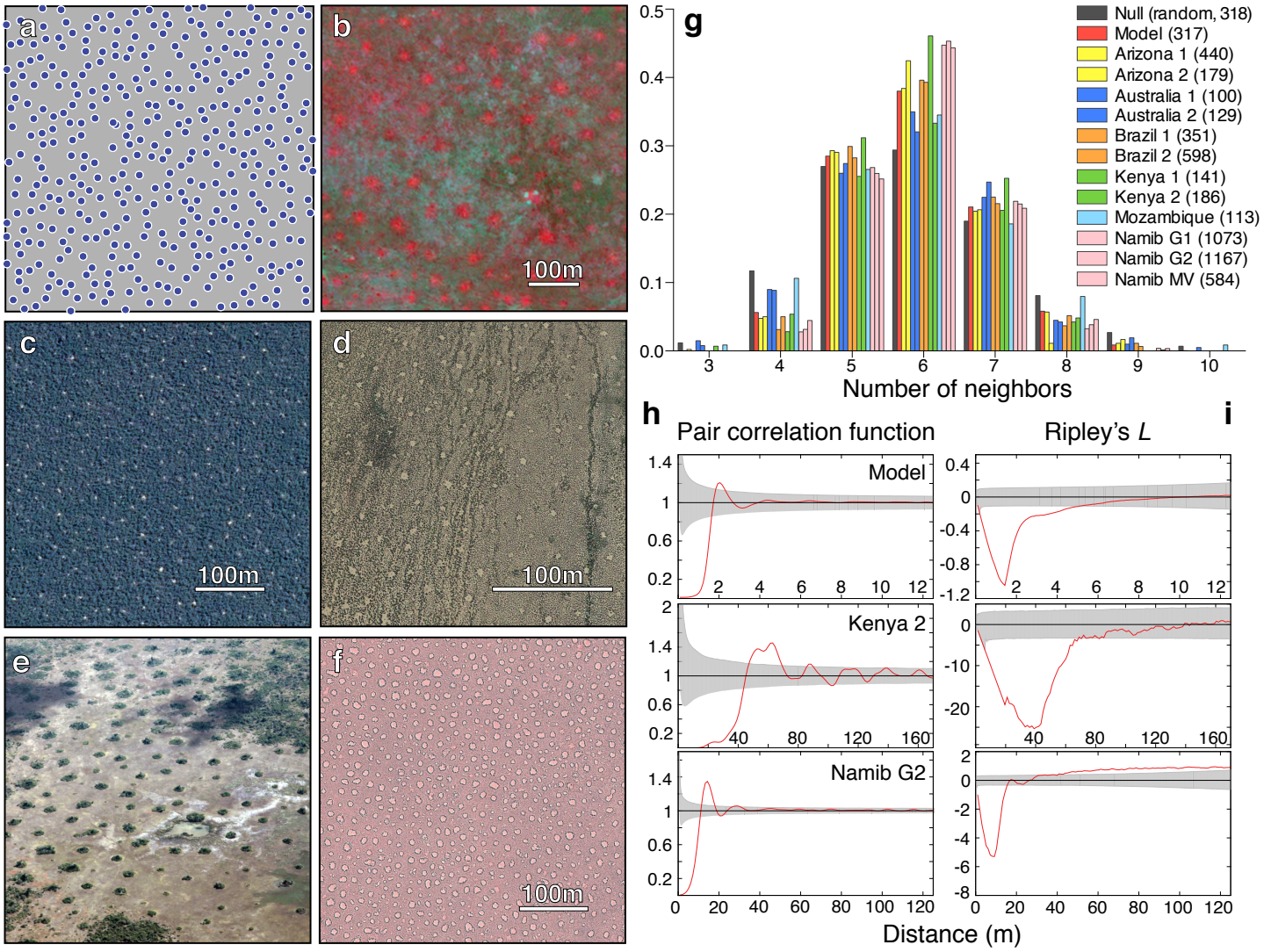
a
b
100m
c
100m
d
100m
e
f
100m
g
Null (random, 318)
Model (317)
Arizona 1 (440)
Arizona 2 (179)
Australia 1 (100)
Australia 2 (129)
Brazil 1 (351)
Brazil 2 (598)
Kenya 1 (141)
Kenya 2 (186)
Mozambique (113)
Namib G1 (1073)
Namib G2 (1167)
Namib MV (584)
Number of neighbors
h
Pair correlation function
Ripley's L
i
Model
Kenya 2
Namib G2
Distance (m)

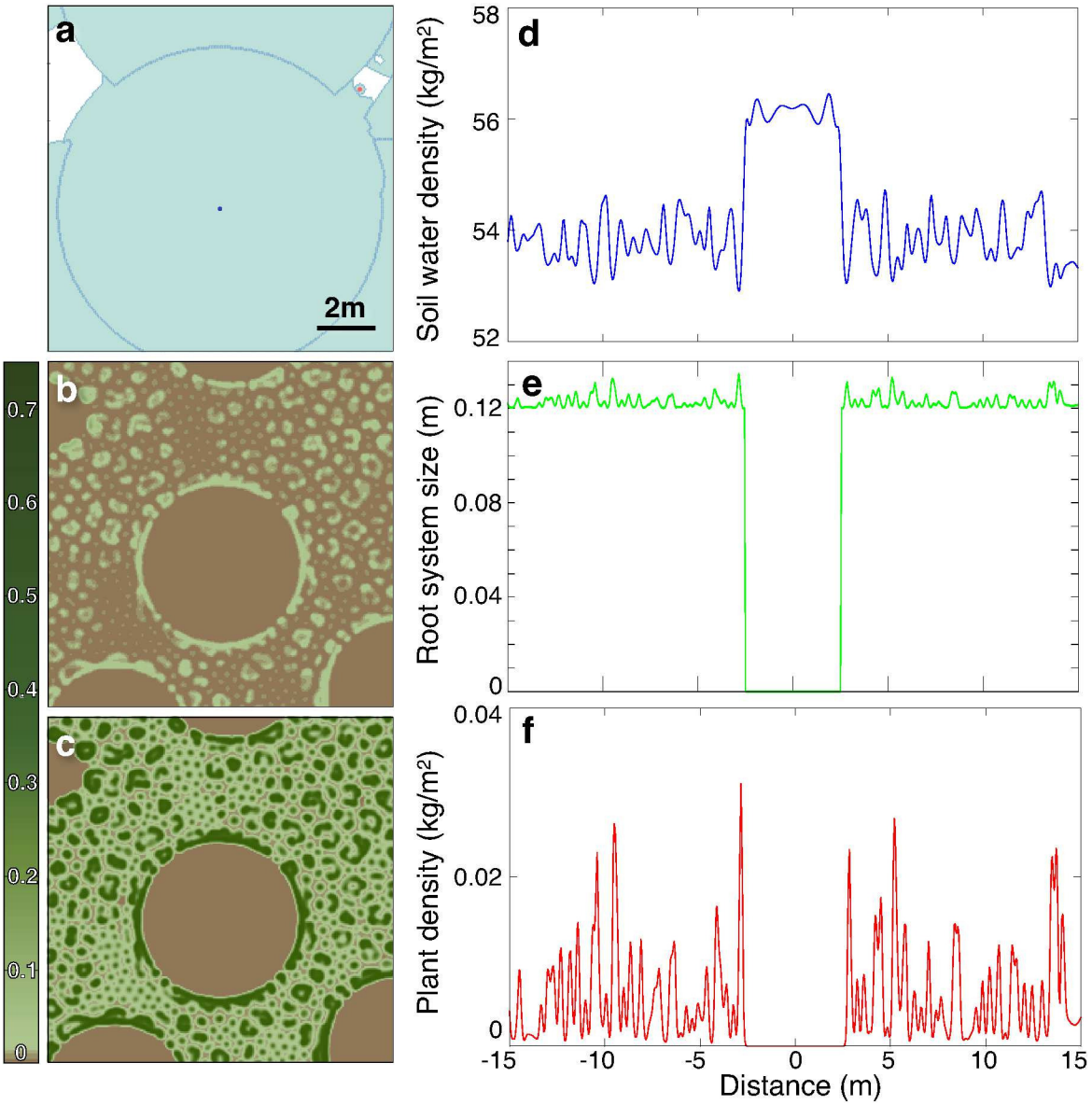
a
2m
b
c
0.7
0.6
0.5
0.4
0.3
0.2
0.1
0
d
Soil water density (kg/m²)
58
56
54
52
e
Root system size (m)
0.12
0.08
0.04
0
f
Plant density (kg/m²)
0.04
0.02
0
-15
-10
-5
0
5
10
15
Distance (m)

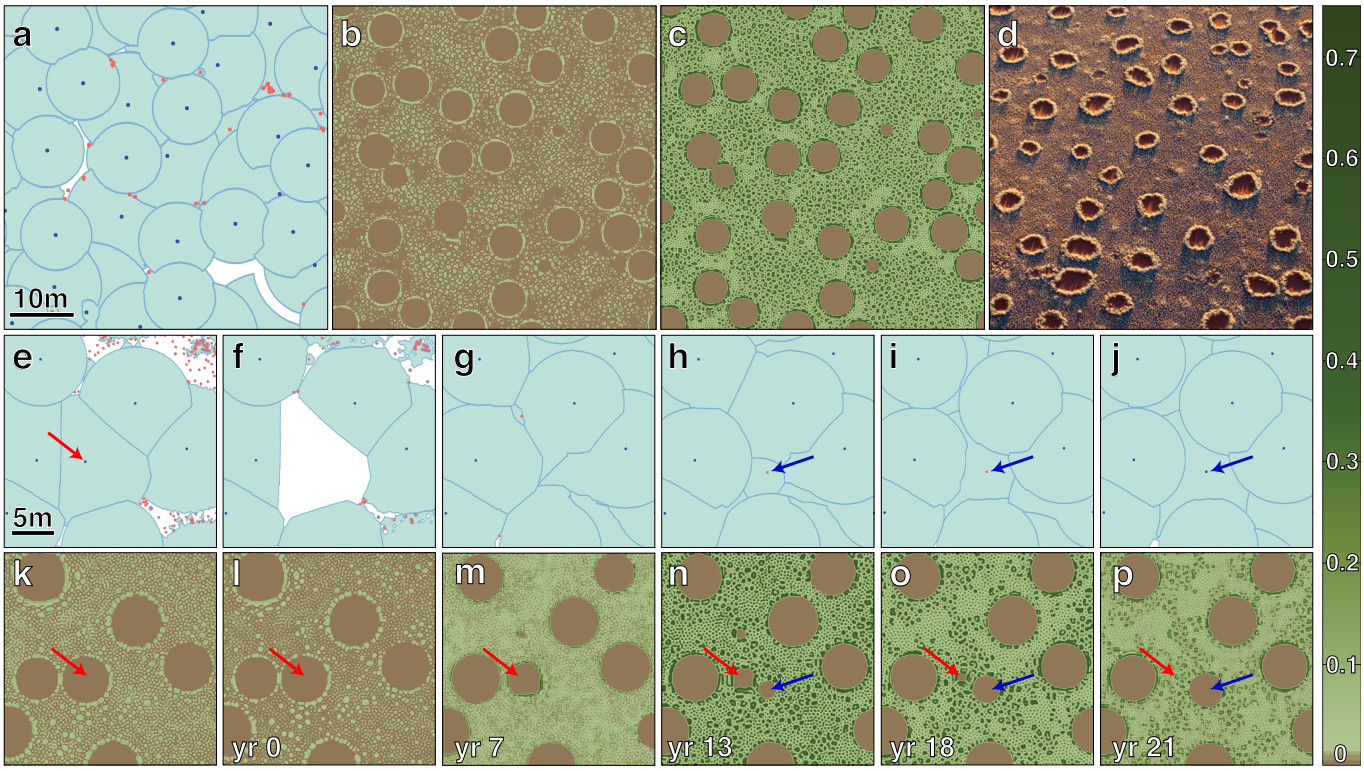
a
b
c
d
10m
e
f
g
h
i
j
5m
k
l
m
n
o
p
yr 0
yr 7
yr 13
yr 18
yr 21
0.7
0.6
0.5
0.4
0.3
0.2
0.1
0

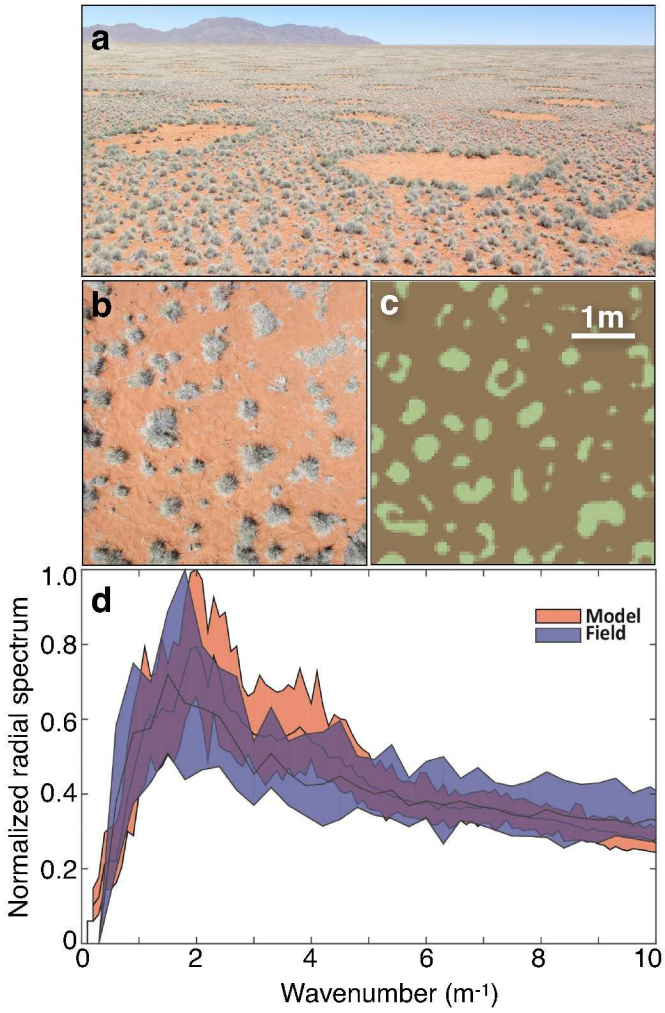
a
b
c
1m
d
Model
Field
Normalized radial spectrum
1.0
0.8
0.6
0.4
0.2
0
0
2
4
6
8
10
Wavenumber (m-1)

Supplementary Information for

A theoretical foundation for multi-scale regular vegetation patterns

Corina E. Tarnita[1,2,*], Juan A. Bonachela[3,*], Efrat Sheffer[4], Jennifer A. Guyton[1], Tyler C. Coverdale[1], Ryan A. Long[5], Robert M. Pringle[1,2]

correspondence to: ctarnita@princeton.edu, juan.bonachela@strath.ac.uk

This supplement contains detailed descriptions of the self-organization models for termites (section 1), vegetation (section 2), and termites and vegetation combined (section 3), along with methods and protocols for collection of empirical data (section 4) and data analysis and comparison with model outputs (section 5). Our models apply generally to territorial, central-place-foraging social insects; throughout the below, however, we refer interchangeably to "termites" (in lieu of the more generic "social insects"), both for convenience and because most of the empirical systems under investigation (and hence our parameterizations) involve termites.

1. Termite self-organization model

To characterize the emergent spatial organization of termite nests, we developed a general mechanistic model for termite colony growth, reproduction, foraging behavior, and intraspecific competition. For computational convenience, we update these dynamics on a yearly basis. The basic elements of the model are:

Landscape and initial condition. We consider a finite landscape consisting of a regular square lattice—i.e., an $N \times N$ grid mesh with discrete positions (sites) equally spaced by a horizontal distance dx and a vertical distance $dy=dx$. This discretization, which uses a very fine spatial grain relative to the landscape and to colony sizes (Extended Data Table 1), allows for considerably faster simulations without, in our case, any loss of accuracy (see sensitivity analysis discussion immediately prior to section 1.1 below). As the initial condition, a single colony founds a nest at a random location within the grid, with a starting population of 2 termites (queen and king) and a minimum viable foraging area $A_{\min}$. This inaugural colony grows, reproduces, and seeds the rest of the system with new incipient colonies; the system develops with time according to the rules detailed below.

Colony. Each colony, i, is characterized by its population biomass, $B_i(t)$, and total foraging-territory area, $A_i(t)$. Because we assume the biomass of each individual to be equal and constant (B_{ind}), keeping track of the population biomass also provides the trajectory of the number of individuals for the colony, i.e. colony size or population size (see full list of parameter values and units in Extended Data Table 1).

Foraging territory area. Termites forage outward from the nest, which is situated at the center of the initial territory. Thus territories expand in a circular fashion; however, because expansion in certain directions may be blocked by other colonies (see *Competition*), territory shape does not necessarily remain circular or centered on the nest proper. $R_i(t)$ denotes the largest radial distance

within the territory, measured from the nest center; this radius is constrained physiologically by R_{max}, the maximum distance that a foraging termite can travel.

Nest. We assume that the physical nest proper occupies a circular area, $M_i(t)$ (centered at the center of the initial territory), whose radius is a certain fraction of $R_i(t)$ given by f_m:

$$M_i(t) = \pi \left(f_m R_i(t) \right)^2 \qquad (1)$$

Colony growth. Consistent with empirical data[31], we assume that termite colonies grow logistically. We model colony size and growth in terms of biomass. Thus, the colony population growth rate reaches a threshold beyond which increasing biomass reduces production (i.e., the more workers there are, the fewer get produced). In addition, we include a per capita mortality rate m:

$$\frac{dB_i(t)}{dt} = \mu B_i \left(1 - B_i \Big/ B_{\max} \right) - mB_i \qquad (2)$$

Production of new colony members (i.e., colony biomass growth), μ, is determined by the queen's constant rate of egg-laying. The carrying capacity, $B_{\max}$, represents the maximum possible biomass that a colony can reach, a limit that we assume to be imposed by intrinsic physiological constraints (e.g., how big a nest structure the colony can construct) and thus equivalent for all colonies. In our model, this limit is never realized due to worker mortality. The effective carrying capacity is therefore $B_{\max}(1-m/\mu)$.

To meet basic energetic maintenance costs and achieve growth, colonies require resources. Specifically, the resources *needed* to maintain colony i at size $B_i(t)$ are given by:

$$\rho_i^{\text{need}}(t) = \frac{1}{c} B_i(t) \qquad (3)$$

where c is the termite assimilation capacity (i.e., the conversion factor from resource biomass into termite biomass). This resource requirement is to be compared with the resources available in the foraging territory (see below). Since we model termites that feed exclusively on dead plant material, we assume that resource availability for colony i at time t at any given location x within that colony's territory is equal to the amount of dead plant material that has accumulated at that location during the previous year (because we update the termite dynamics annually, each location within a territory belongs exclusively to one colony throughout the whole year). Assuming that plant mortality occurs at a constant rate, m_P, and given that colony i occupies area $A_i(t)$ at time t, the resources *available* to colony i, $\rho_i(t)$, are:

$$\rho_i(t) = \int_{A_i(t)} \int m_P \cdot P(\vec{x}, t') dt' d\vec{x} \qquad (4)$$

where $P(x, t)$ is the live plant biomass at location x and time t. In Section 3, we will model vegetation dynamically; however, in this section we assume a simplified scenario in which the

system-wide plant biomass is invariant and uniformly distributed in space; that is, $P(x,t) = P_{cst}$, a constant. To achieve this, we assume that $P(x,t)$ regenerates instantaneously and is kept at P_{cst} (except on nests, see *Termite engineering*).

Because termite dynamics are updated annually, resource requirement and availability are compared at the beginning of each year. If $\rho_i \neq \rho_i^{need}$, the colony will try to adjust its foraging territory accordingly: if resources are insufficient ($\rho_i < \rho_i^{need}$), the colony will expand its foraging territory trying to obtain the necessary resources; conversely, if resources are in excess ($\rho_i > \rho_i^{need}$), termites will not need to travel as far to harvest the minimum necessary resources, and the foraging territory will shrink. Such shrinkage produces "empty" (unoccupied) area potentially available for nearby colonies as additional foraging territory.

Thus, Eqs. (3) and (4) establish a link between changes in colony biomass and the corresponding change in foraging territory size, which in turn modifies the colony's largest radial distance $R_i(t)$. Because this radius is the largest distance that colony i travels for forage, we assume that, if at any time new contiguous space becomes available within distance $R_i(t)$ from the center of the colony in any direction, the colony will attempt to occupy it. If the incorporation of this additional territory leads to an accumulation of resources in excess of ρ_i^{need}, the territory will shrink starting from the outermost locations, until $\rho_i = \rho_i^{need}$. Because seeking an exact match of both quantities would lead to an infinite computational loop of territory addition and removal, we allow for a certain margin of difference between the two (here, this margin is set using the territory border—specifically, the amount of resources found at the discrete locations that compose the territory boundary). Colonies will always preferentially use the closest available space to form their foraging territory.

If territory expansion is hindered for any reason (e.g., lack of available space, or R_{max} being reached), then colony biomass will grow only as much as allowed by the resources available up to the point of hindrance.

Territorial competition. If territory expansion leads to overlap with the territory of another colony, we assume that a conflict ensues at the border between the two territories in the form of direct interference competition, avoidance, and/or aggressive territorial defense (such agonism between intraspecific colonies is common among many, perhaps most, species of termites and ants[29,32]). These conflicts can simply remain as border skirmishes (i.e., offsetting mortalities, neither colony gains any net ground) or can lead to "wars" that may result in the extermination of one colony. We assume that smaller, growing colonies exhibit more aggressively expansionist tendencies than do larger established ones, in keeping with evidence that aggression declines with distance from the nest[33] (Extended Data Fig. 1a):

$$\Pr(i \text{ and } j \text{ at war}) = \Pr(i \text{ seeks war}) \times \Pr(j \text{ seeks war}),$$

where:

$$\Pr(i \text{ seeks war}) = \frac{1}{1+e^{-\beta_2(1-\alpha_2 S_i(t))}}, \qquad \text{with} \qquad S_i(t) = \frac{B_i(t)}{B_{\max}} \tag{5}$$

War results either in the death of one colony (highly probable if there is a substantial size discrepancy since we assume ~1:1 mortality in conflict) or in coexistence (if sizes are similar), in which case the workers' foraging radius is truncated, a boundary is established, and expansion ceases in that direction. If colonies i and j fight, then i wins with probability:

$$\Pr(i \text{ beats } j) = \frac{1}{1+e^{-\beta\left(1-\alpha S_j(t)/S_i(t)\right)}}, \quad (6)$$

where α is a parameter that determines the size difference at which the probability that i wins is 0.5, and β is a parameter that determines the sensitivity of the war outcome to small differences in colony size (higher β means stronger effects of small size differences). By symmetry, j wins with probability Pr(j beats i); with the remaining probability, there is no winner and the two colonies coexist. Examples of the probability functions above are shown in Extended Data Fig. 1b.

If colony i dies in conflict, the winning colony j also suffers losses in the form of reductions in both territory and population biomass: $A_j' = A_j - A_i$, and B_j is reduced proportionally [i.e. $B_j' = B_j (A_j'/A_j)$]. Shrinking occurs in a way that maintains the original shapes of territories, but the growth rules above ensure that territories recover circularity as soon as sufficient space becomes available. In the rare event that the winning colony has a smaller territory and biomass than the losing one, then both territory and population biomass are decreased to a fraction q of the original: $A_j' = qA_j$. In either case, the winning area cannot be reduced below the minimum starting area, $A_{\min}$.

These probabilistic conflict rules do not apply in the case of a colony being completely surrounded by the territory of another colony. In that case, the smaller (engulfed) colony dies with probability 1.

Reproduction. We assume that when colonies reach a certain population biomass, $B_{\text{mat}} < B_{\max}$, they become reproductively mature (a.k.a. established) and produce alates (winged dispersing future queens and kings) as follows. If, during the current time step, colony i shrinks in biomass due to resource limitation, then it forgoes reproduction even if its newly reduced biomass exceeds B_{mat}; otherwise, it produces a number of alates proportional to a fraction f_A of its biomass. In our simulations we assume that these alates disperse randomly and in pairs over the entire grid, since our maximum grid size (51.2x51.2m) is smaller than the typical distances that termite alates are known to disperse (often >100m;[61,62]).

If an alate pair lands within the territory of an established colony or does not have enough space to initiate (i.e., available area at the landing point < A_{min}), the alates die. Otherwise, they start a new colony. The landing point is assumed to be the center of the new nest.

Mortality. There are two sources of mortality for colonies. The first is conflict between neighbors (see above), which we assume to be the primary cause of death in small colonies, but to decline in importance as colonies grow. Indeed, empirical observations from multiple systems suggest that territorial conflict eliminates many incipient colonies but seldom leads to the death of a mature colony, whereas mature colonies show signs of perpetual conflict at outer edges of

their foraging territories[34-36]. The second source of mortality is an intrinsic stochastic death rate, which primarily affects established colonies. We let m_C be stochastic mortality for large colonies and set it to replicate a realistic lifetime for mature colonies, based on values from the literature[31,37] (Extended Data Table 1).

Termite engineering. As explained in the main text, termites frequently either enhance or suppress the growth of vegetation on nests or cause plant mortality[3,4,63,64]. We have previously modeled the former scenario (enhancement), assuming an exogenously imposed, regularly patterned template of termite nests[4]. Here, we focus on the scenario in which termites locally deplete plant biomass, as hypothesized for the sand termite *Psammotermes allocerus* (Rhinotermitidae), which has been suggested as the cause of the Namib fairy circles (FCs)[7]. On nests, we assume the mortality rate of plant biomass to be elevated by a fixed proportion ν:

$$m_{P_{off}} = m_P; \qquad m_{P_{on_i}} = \nu\, m_{P_{off}}; \qquad (7)$$

In the simple resource scenario implemented in this "termite-only" dynamic model, we assume this factor to be large enough to completely eradicate the vegetation on nests, and to prevent it from regenerating[7]. In light of observational and experimental data showing that *P. allocerus* enhances grass mortality by browsing roots but do not consume aboveground plant parts[8,28], we likewise assume that termites do not consume the grass that they kill on nests and omit this biomass quantity from the calculation of resource availability in Eq. (4). This assumption does not qualitatively influence our results.

Parameterization. We aimed to parameterize the model realistically. We consulted the literature to identify plausible (and internally consistent) values of individual-, colony-, and population-level parameters such as termite individual biomass, population density and growth dynamics, and thresholds for maturity and reproduction (Extended Data Table 1). Again, because one specific use of this model was to study the Namib FCs, we sought parameter values consistent with what is known about *P. allocerus*[7]. However, because little is known about the biology of this species, we also consulted the wider termite literature when necessary. In so doing, we tried to select broadly representative (i.e., not extreme or outlying) values, and to use data from congeneric *Psammotermes* or confamilial Rhinotermitid species when possible (where appropriate, references are provided alongside parameter values in Extended Data Table 1). For example, the biomass conversion factor, c, a ratio of production:consumption (Extended Data Table 1), was calculated from data on annual termite colony production (0.111g m^{-2} yr^{-1}) and biomass consumption (1.58 g m^{-2} yr^{-1}) for Sahelian *P. hybostoma*[50].

However, we know of no published data that would enable us to derive accurate quantitative values for several parameters associated with functions that are key to the model. They include parameters related to colony competition (e.g. α, β, etc.). For these, we used biologically plausible arguments and anecdotal field observations to select parameter values that we consider realistic.

Finally, a few parameters were set by computational considerations and have little impact on the results: minimum area (A_{min}), time step (annual), grid mesh ($dx = dy = 0.05$ m), system size (1024 sites). We conducted a sensitivity analysis to verify that neither the chosen spatial

grain nor the topology of the discretization affected our results. We reduced grid cell size (dx = 0.025m versus dx = 0.05m) and tested both square and hexagonal grids (the latter allows densest packing of circles in two dimensions, and therefore provides the closest approximation of continuous space). The resulting spatial distribution of colonies was indistinguishable across the different choices, and we found no appreciable quantitative or qualitative differences in the spatial analysis of the resulting patterns.

1.1 Results

To study the dynamics emerging from the rules above, we used a 51.2×51.2m system (1024×1024 site grid) under six different resource scenarios, namely P_{cst} = 1, 0.5, 0.2, 0.1, 0.05, and 5×10^{-3} Kg m^{-2}. For each scenario, we compiled spatial and temporal information corresponding to either all colonies or mature colonies only, averaged over 100 simulations. We monitored change through time in mean nest diameter (Extended Data Fig. 2a), mean distance between neighbor colonies (Extended Data Fig. 2b), total number of colonies, mean termite biomass per colony, and realized resource density per colony (average ρ_i/A_i, Kg m^{-2}). On average, the system reached stationarity (fluctuating around a well defined constant average) after ~200 years (Extended Data Fig. 2a,b). Thus, although the stochastic mechanisms included in the model naturally introduce fluctuations, there was a well-defined stationary average for these metrics across replicates (i.e. across realizations of the dynamics using different initial conditions). We measured this stationary average across replicates for all the metrics above to evaluate their dependence on (annually) available resources (see Extended Data Fig. 2c-f). The stationary termite biomass density (B_i/A_i, g/m^{-2}) and, therefore, termite population density ($(B_i/B_{ind})/A_i$, individuals m^{-2}) increase with P_{cst} (Extended Data Fig. 2e). Biomass (and implicitly number of individuals per colony) increases with resource availability and saturates at the realized carrying capacity, $B_{\max}(1-m/\mu)$ (see Eq.(2)). Under low resource availability, colonies never reached this maximum potential due to the effects of territorial competition and conflict (Extended Data Fig. 2f). Competition for space is stronger at lower resource availability, because colonies require larger foraging territories (Extended Data Fig. 2c); consequently, the nearest-neighbor distance increases as resource availability decreases (Extended Data Fig. 2d).

At the stationary state, we analyzed the spatial distribution of mature colonies, using two standard indicators[41]. First, we used the pairwise correlation function (PCF), $g(r)$, which essentially measures the probability of finding colonies separated by a certain distance r. In the PCF, $g(r) = 1$ when the point distribution shows complete spatial randomness (CSR, equivalent to the expectation under a homogeneous Poisson process) for a given r; values <1 indicate regularity at that distance; and values >1 indicate aggregation. Thus, curves that show "peaks" of aggregation followed by "valleys" of regularity indicate ordered spatial distributions. Second, we used Ripley's L function, which is a cumulative function of the PCF and thus provides similar information but less prone to noise[41]. Here we use a shifted version of the function for which $L(r) = 0$ indicates CSR, $L(r) < 0$ indicates overdispersion, and $L(r) > 0$, aggregation. For these analyses, we used results from the high resource density scenarios (e.g. 1 Kg m^{-2}), as these had sufficient nest densities to reliably compute these functions. We used both the "spatstat" package[41] in R and our own Fortran code to calculate both $g(r)$ and $L(r)$. We also used R's "spatstat" for the calculation of significance envelopes: parts of the curves that fall outside these

envelopes indicate that the behavior of the system is significantly different from CSR for that specific distance *r*.

Both indicators revealed statistically-significant overdispersion in nest distribution (Fig. 1h). Ripley's *L* shows the characteristic "regularity valley" for distances just under those where the PCF shows a peak followed by a valley. Furthermore, the probability distribution for the number of neighbors (which is remarkably insensitive to resource availability changes; Extended Data Fig. 2g) consistently shows ~6 as both the mean and modal number of neighbors for a colony (Fig. 1G, Extended Data Fig. 2g inset), indicating a hexagonal distribution of colonies. In summary, our general model for intraspecific competition between termite colonies leads to the emergence of large-scale self-organization of the nests into a nearly hexagonal lattice pattern.

2. Vegetation self-organization model

Beginning in this section, we focus specifically on the Namib desert. For the vegetation dynamics, we chose a model that has been used repeatedly by other authors to describe and reproduce the patterns of self-organization that are typical of vegetation in semi-arid environments (including the one in the Namib desert)[15]. The model considers the dynamics of vegetation, *P*, soil water, *W*, and surface water, *O*, densities. In a nutshell, plants grow thanks to soil water uptake, soil water results from the infiltration of surface water, and surface water results from the accumulation of rainfall. Assuming a flat terrain, the model can be written as:

$$\frac{\partial P(\vec{x},t)}{\partial t} = G_P(\vec{x},t)P(\vec{x},t)\left(1 - P(\vec{x},t)/K\right) - m_P P(\vec{x},t) + D_P \nabla^2 P(\vec{x},t) \qquad (8)$$

$$\frac{\partial W(\vec{x},t)}{\partial t} = \gamma \frac{P(\vec{x},t) + QW_0}{P(\vec{x},t) + Q} O(\vec{x},t) - N\left(1 - R_{educ} P(\vec{x},t)/K\right) W(\vec{x},t) - G_W(\vec{x},t) W(\vec{x},t) + D_W \nabla^2 W(\vec{x},t) \qquad (9)$$

$$\frac{\partial O(\vec{x},t)}{\partial t} = R_{ainfall} - \gamma \frac{P(\vec{x},t) + QW_0}{P(\vec{x},t) + Q} O(\vec{x},t) + D_O \nabla^2 \left(O^2(\vec{x},t)\right) \qquad (10)$$

where ∇^2 represents the nabla operator (second spatial derivative) and the values and meaning of parameters can be found in Extended Data Table 2. The first term in Eq.(10) represents rainfall, the second term represents infiltration of surface water into the soil, and the third term represents water (superficial) diffusion. The first term in Eq.(9) represents the increase in soil water due to infiltration, whereas the second term represents evaporation, the third term represents soil water uptake, and the last term soil water diffusion. Lastly, the first term in Eq.(8) represents plant growth due to water uptake, the second term represents mortality, and the third term vegetation biomass diffusion (via e.g. seed dispersal). In turn, G_P and G_W, plant growth rate and soil water consumption rate respectively, depend on the extension of the root system. Thus, if the root system is encoded in the kernel:

$$G(\vec{x},\vec{x}',t) = \frac{1}{2\pi S_0^2} \exp\left[- \frac{\left|\vec{x} - \vec{x}'\right|^2}{2\left[S_0\left(1 + EP(\vec{x},t)\right)\right]^2} \right], \qquad (11)$$

the effect of roots on growth and water consumption, respectively, is given by:

$$G_P(\vec{x},t) = \Lambda \int_L G(\vec{x},\vec{x}',t) W(\vec{x}',t) d\vec{x}' \qquad (12)$$

$$G_W(\vec{x},t) = \Gamma \int_L G(\vec{x}',\vec{x},t) P(\vec{x}',t) d\vec{x}' \qquad (13)$$

where the integrals consider the totality of the system[1] [38]. The kernel therefore determines to what extent roots from a body of vegetation biomass (e.g. clump) can use water from (Eq.(12)) and influence (Eq.(13)) other parts of the system. Specifically, the Gaussian kernel above sets this distance through its standard deviation, the root-system size, given by $S_0(1+EP(x,t))$.

On the other hand, due to the large infiltration levels characteristic of the Namib desert sandy soil, we approximate the infiltration contrast parameter (W_0) to be close to its maximum value (unity). For the same reasons, we consider the surface water diffusivity (D_O) to be negligible (Extended Data Table 2). Therefore, most of the surface water variation necessarily results from variability in rainfall levels ($R_{ainfall}$). In contrast to most models for self-organized vegetation patterns in this region, which assume rainfall to be constant through the years, here we use a rainfall function that varies on small timescales. Specifically, we used data from 2004-2014 from multiple Namib desert locations (provided by Vanessa Hartung) to calculate mean monthly rainfall in a "average" year along with standard errors reflecting among-year variation in monthly totals. The resulting $R_{ainfall}(t)$ depicts the two distinct seasons (wet and dry) characteristic of this region (see Extended Data Fig. 5):

$$R_{ainfall}(t) = R_0 10^{\omega \sin\left(\frac{(t+1)\pi}{6}\right)} \left[1 + \sigma_R \eta(t)\right] \qquad (14)$$

Here, t is the month of the year, and the second term in brackets represents noise (random number uniformly distributed between 0 and σ_R) that takes into account an additional source of stochasticity inherently associated with the weather. The form of the noise ensures that the highest variability occurs during the rainy season, in agreement with the larger variances in the data during that season. Note that, rather than trying to represent the rainfall time series for the specific years 2004-2014, our rainfall function attempts to reproduce characteristic year-to-year rainfall patterns in NamibRand, with the standard errors around the means for each month being used to reproduce realistic stochastic variability in that expectation. Moreover, as detailed in the final subsection of section 3 below, we have also gone beyond the range of these data by simulating rainfall levels that depart significantly from this average behavior for a prolonged amount of time.

Parameterization. The equations above, including the time-dependent rainfall function, are parameterized following data when available, or biological arguments otherwise. As a starting point, we used the parameterizations from[9,10,15], which we modified in order to tailor the

[1] In order to deal with such system-wide kernels, we follow the methodology explained in XXX, which uses an approximated version of the Gaussian kernel in Eq.(9) that transforms Eq.(10) and (11) into a regular convolution integral, thus allowing for the use of the convolution theorem to speed up the numerical calculation of both integrals.

parameterization to the focal system (the Namib desert) when more appropriate data or arguments were available (e.g. W_0 close to *1* and D_O=*0*). The main modifications arise because, ultimately, the chosen parameterization needs to be able to replicate two important features observed in the Namib desert vegetation along the year: *i)* large variation in biomass between dry and rainy season, and *ii)* clumps of vegetation of small size (radius around 20-30cm). This latter feature is identified in our new field data (see data sections below), and therefore never considered in previous parameterizations of such models. The resulting set of parameters can be found in Extended Data Table 2. For the simulations of this vegetation-only model, we used system sizes ranging from 6.4x6.4m to 51.2x51.2m (128x128 to 1024x1024 grid sizes, respectively). Following standard implementations for these models[9,38,65], we used an underlying square lattice to discretize space with a mesh of $dx = dy = 0.05$m.

2.1 Implementation of an asymmetric root system

One important feature of the vegetation model above is that the root system represented by the Gaussian kernel, Eq.(4), is symmetric and therefore root density is equivalent in all directions, regardless of heterogeneities in water availability. However, desert-plant roots in sandy substrates both (a) grow preferentially in the direction of localized moisture concentrations (hydrotropism) and (b) exhibit enhanced proliferation, branching, and biomass growth in moist vs. dry soil, breaking the symmetry of root architecture in ways thought to enable "precise exploitation of water patches and drought avoidance)[38]. We therefore modified the above model to incorporate the possibility of hydrotropism and asymmetric root proliferation (or asymmetric exploitation of soil moisture) in response to localized differences in soil-water availability. Once the soil-moisture difference dissipates, the root system in that direction returns to its original growth pattern.

More specifically, we introduced an additional term in the plant growth equation, Eq.(8), that modifies plant growth rate by a specific factor. This is calculated by adding to the existing term $G_P(x,t)$, an additional contribution from any direction in which soil water surpasses a site-specific threshold, W_{th}:

$$\widetilde{G}_P(\vec{x},t) = G_P(\vec{x},t)\left[1 + \omega F_{asym}(\vec{x},t)\right] \qquad (15)$$

where ω is a (dimensionless) diminishing factor (in our simulations, $\omega = 0.5$), necessary to prevent numerical instabilities leading to unrealistic features such as system-wide plant clusters, and F_{asym} is the improvement function *per se*, given by:

$$F_{asym}(\vec{x},t) = \left\langle \frac{W(\vec{x}',t)}{W(\vec{x},t)} \right\rangle_{\vec{x}'} \qquad (16)$$

The <…> symbol represents spatial averages as follows: following Eq.(11), the standard deviation of the Gaussian root system is given by $S_0\left(1 + EP(\vec{x},t)\right)$; therefore, a rough estimate of the maximum length of the root system is given by three times that standard deviation. Thus, the spatial averages in Eq.(16) consider locations at a distance:

$$|\vec{x} - \vec{x}'| \approx 3S_0\left(1 + EP(\vec{x},t)\right) \quad (17)$$

and use the immediate neighborhood of these locations to assess the average water availability and how different it is from $W(\vec{x},t)$. Because our simulations occur on a square lattice, such spatial average only considers the 4 neighbors of a location *x'*. However, only nearest neighbors of *x'* fulfilling:

$$\frac{W(\vec{x}'_{nn},t)}{W(\vec{x},t)} - W_{thr} > 0$$

are considered for the average, which ensures that only a sufficiently large contrast between the focal location *x* and the neighborhood of *x'* triggers this differential root growth. In our simulations, we set W_{th}=4.

In summary, Eq.(16) detects large differences in water availability in the neighborhood immediately outside the symmetric root kernel, and Eq.(15) considers the improvement in growth rate contributed by each direction where that happens. We assume that the local removal of water from these elongated directions does not have a significant effect on G_W. Because our modifications to the growth-rate kernel are devised to illustrate the potential qualitative and quantitative change of introducing the additional asymmetric mechanism, we parameterized the threshold (W_{thr}) and consequent boost in growth rate (F_{asym}) using values on the upper range of possible values, in order to obtain clear effects from potential local water differences. A careful study of how the root system grows differentially, as well as a parameterization that takes into account in-situ measurements, would provide much more accurate results.

2.2 Results

Symmetric root system. As explained above, the vegetation model with a symmetric root system has been intensely studied in the past. As a result, it is well known that this model is able to show the typical spatial self-organized patterns of vegetation, namely spotted vegetation, labyrinths, and gaps, when the rainfall level is between the desertification threshold and the homogeneous-vegetation threshold. For a given parameterization, when the rainfall parameter is fine tuned to a specific value between those thresholds, the stationary homogeneous non-trivial state is unstable under non-periodic perturbations, and the feedbacks present in the system give rise to one of these (rainfall-dependent) patterns[15].

When rainfall is fine-tuned, the Namibia-specific parameterization actually entails a reduction of the range of fixed rainfall for which the system shows pattern formation, in comparison with generic parameterizations available in the literature[10,15] (for the parameterization in Extended Data Table 2, the range of rainfall between spots and gaps is only ~75mm/yr). Note that some of the changes we introduce in the parameterization typically used for Namibia, specifically setting W_0 close to 1 and D_O to 0, affect directly some of the main pattern-related feedbacks in the model, and therefore may prevent Turing-like patterns from emerging.

We further ran a sensitivity analysis in small 6.4x6.4m systems to understand and quantify the effect of changes in each of the remaining parameters in Extended Data Table 2. Although the behavior of the different components of the model has been studied in the past[15], there were two remarkable results unveiled by our analysis that are relevant for our study. First, the parameters associated with the Gaussian kernel, Eq.(11), turned out to be intimately related to the scale of the emerging patterns. Also important for any computational project is the study of the dependence of results on the system size; in our case, sizes below 25.6x25.6m are subject to finite-size effects that, although do not alter the qualitative results (e.g. type of pattern), do change considerably the quantitative result, e.g. the average levels of vegetation biomass density (results not shown).

Thus, fixed levels of rainfall allowed us to better understand and calibrate the vegetation model. However, henceforth we study the model above using the variable rainfall function introduced in Eq.(14), in order to monitor the emergent changes in the distribution of vegetation for the specific case of the Namib desert. The narrowed pattern range offered by our parameterization does not prevent the system from showing realistic (spot-like) patterns when the fixed rainfall parameter is replaced by the variable rainfall function above (Eq.14). This is a nontrivial result, given that the rainfall levels reached by this function using Namib-specific values range from 0 to values well within ranges for which homogeneity is expected. The system moves from big, dense clumps of vegetation when rainfall reaches its maximum levels in February, to almost inexistent levels in the dry season. Although the total spatial average level of vegetation ranges from 0.001 Kg/m^2 to 0.1 Kg/m^2, vegetation can reach locally peaks of approximately 0.5 Kg/m^2.

Asymmetric root system. When the asymmetric root mechanism, Eq.(15), was included in simulations of the vegetation-only system, the resulting behavior for the dynamic equilibrium was barely influenced (Extended Data Fig. 6a,b). Although, during the transient to that stationary state, the system does show some sparse clumps of a bigger size, the final pattern is composed of identical (small) clumps distributed regularly in the system. This stationary pattern is indistinguishable from the symmetric case pattern.

3. Termite-vegetation coupled model: the case of Fairy Circles (FCs)

In the past, FCs have been hypothesized to be the result of termite action[7], or the emergent result of vegetation-water interactions[9,10]. Importantly, the latter hypothesis has been introduced using scale-dependent feedback (SDF) models such as the vegetation model above, trying to explain FCs as regularly self-organized bare-soil gaps within an otherwise homogeneously-vegetated system.

As explained in the main text, we hypothesize that fairy circles emerge from the close interaction between termite and vegetation dynamics. Thus, we used a coupled model that brings together the termite and vegetation dynamics above, and therefore considers not only such dynamics but also possible feedbacks between the two ecological components.

Such a coupled model considers the termite dynamic rules explained in section 1, where now the resource density field, $P(x,t)$, (see Eq.(4)) changes with time and space according to the vegetation dynamics from section 2 (Eqs.(8)-(13)). Thus, Eqs. (4), (7) and (8) connect the

vegetation dynamics with the termite dynamics through the plant mortality term. In other words, the model couples termite and vegetation dynamics by using the vegetation density given by the model in the previous section as the only resource for the termites. This coupling will affect nontrivially both termite and vegetation dynamics, influencing vegetation growth and spatial distribution as well as termite growth.

For this coupled model, we used system sizes ranging 25.6x25.6m to 51.2x51.2m. See Extended Data Tables 1 and 2 for the rest of the parameters.

3.1 Results

***One (fixed) colony system; symmetric roots*.** As a first step to understand the influence of termites on the vegetation-water system, we included one single mature colony at the center of a 25.6x25.6m system, with no additional dynamics other than the increased plant mortality (Eq.(7)) occurring on the center of the associated (5 meter) nest; resources are described by equations (8)-(10). In this "naïve" termite-vegetation setup, we studied three different situations: constant rainfall, variable rainfall, and a case in which the colony disappears shortly after the stationary state of the system is reached. In every case, both the mature colony and the initial condition for vegetation are introduced at the same time, and the complete system is allowed to reach a stationary state.

In all cases, the presence of the termite nest was translated into a vegetation gap on top of the nest. With both static and variable rainfall levels, the vegetation around the nest and in the matrix was not significantly different from the vegetation patterns obtained without the colony (Extended Data Fig. 6c), but the amount of soil water accumulated into the gap region due to the absence of plants was much higher than in the matrix. This increased on-nest plant mortality prevents on-nest soil water depletion by the plants.

In addition, we probed whether the vegetation in the system is able to recover after the perturbation (i.e. the colony) disappears, and how long that takes. To this end, we allowed the system to run for 10 years from the initial state to ensure that a stationary state is reached, after which we removed the colony from the system. The gap generated by the (now disappeared) colony was slowly repopulated by vegetation, and thus it was eventually closed. However, we estimated that it would need hundreds of years to do so. The reason for this slow regrowth of vegetation closing the existing gap is that diffusivity (i.e. laplacian) terms in vegetation and resources represent the only mechanisms for the diffusion of plant biomass, and the typical values for the diffusivity constants in this region are very small (see D_P, Extended Data Table 2). Because these parameter values are realistic, the question arises as to whether there is an additional mechanism behind the quick closure of vegetation.

***One (fixed) colony system; asymmetric roots*.** Indeed, when repeating the same set of computational experiments with the system after the asymmetric root mechanism is included, we observed a significant response of the vegetation around the gap (Extended Data Fig. 6d), as well as noticeable effects on the matrix vegetation. This is due to the asymmetric roots, which allow vegetation to access the pool of soil water accumulated in the gap in the absence of plants. Thus, vegetation around the gap quickly develops denser and taller than in the matrix. These denser

clumps contribute to generating water differences among other parts of the system throughout the seasons, and thus the presence of the termite nest eventually translates into some sparse bigger clumps of vegetation in the matrix.

Furthermore, when the colony is removed, the gap closes on in ~20-40 years (Extended Data Fig. 6e,f), as a consequence of the additional asymmetric root mechanism. The enhanced plant performance around the gap influences the diffusivity of vegetation when the colony disappears: the higher contrast between the vegetation around and the vegetation within the gap increases diffusivity in comparison with the previous case, thus allowing the gap to close much faster. Bigger clumps still remain after the gap has fully closed, but will eventually disappear as the large differences in soil water availability between the former bare patch and the matrix also disappear, leaving a system that is indistinguishable from the vegetation-only case.

Dynamic colonies and vegetation system; asymmetric roots. The initial condition for this coupled system is again one single colony, now an incipient one, randomly placed in a system with homogeneous vegetation cover. As before, this vegetation is perturbed using additional, randomly distributed vegetation density. The dynamics of termite colonies (Eq.(1)-(6) and (15)) are coupled to the dynamics of vegetation, including variable rainfall and asymmetric roots, (Eqs.(8)-(14)). After approximately 100 years, both termite colonies and vegetation self-organize dynamically to a steady state in which the resulting emergent spatial pattern for matrix vegetation differs from that obtained with the "naïve" (i.e. one single, static nest) setup. Although the presence of termite nests is equally revealed by gaps in vegetation that match nest shapes and sizes regardless of rainfall, there are important differences in the vegetation behavior throughout the year. In the part of the year during which vegetation is the tallest, regularly organized small clumps of vegetation coexist with heterogeneously distributed bigger ones. The latter result from the interaction between variable rainfall, asymmetry in the root system, and the presence of termite nests, which is revealed by the fact that these big clumps were mostly inexistent in the case of one single, static nest; however, when many (incipient or mature) colonies are present, there is a higher opportunity for differences in soil water availability to arise, therefore allowing for the emergence of more of these bigger clumps. At the same time, this asymmetry mechanism is also responsible for the existence of sparse aggregations of surviving vegetation clumps when vegetation is at its lowest level, which occurs immediately after the dry season. At these stages, asymmetry also allows the (taller) vegetation around the gaps to survive, thus forming a landscape with dispersed clumps in the matrix in addition to what is known as the FCs *per se* (i.e. ring of clumpy vegetation around gaps).

The diameter of the FCs matches that of the termite nests (since this is our simplifying assumption). The termite dynamics and interaction with the vegetation dynamics give rise to an emergent value that, for our parametrization and considering only mature FCs at the steady state, remains around 5.4m (results not shown). The distance between touching neighbor colonies stabilizes around 10m, and the average annual vegetation density per unit area of a colony, $<\rho(t)>$, around 0.51Kg/m^2. The population density also reaches its effective carrying capacity. The size of the FC and the density of vegetation forming the perennial belt determine the closure time of relic FCs after colony death: relic FCs resulting from the death of mature colonies require on average 19.3±1.6 years to close with our parametrization. Importantly, the different sources of variability in our model lead to broad distributions for both closure time and colony lifetime

(main factors determining FC life span). Therefore, the distribution of FC lifetimes is also broad, ranging from a <5yrs to >165yrs (see Extended Data Fig. 8). This distribution was derived by tracking all FCs (n = 53) that were born (i.e., appeared as a noticeable gap) at the stationary state of the merged model simulations and disappeared (i.e., indistinguishable from matrix) during the simulation. Because simulations ran for ~170 years after reaching stationary state, the distribution of lifespans is unavoidably truncated at lifespans > 170 years. Although this truncation may alter slightly the average lifespan, we do not expect it to considerably skew the shape of the distribution, as the different sources of mortality prevent the great majority of colonies from living so long. Indeed, long-term simulations (>500 years) of the termite-only model reveal that most incipient colonies disappear before even forming a noticeable FC, whereas no colony lived longer than 200 years (results not shown). Given the average closure time of ~20 years following colony death, this suggests that the merged simulation is unlikely to yield FCs living >220 years.

Response of the ecosystem to different stress levels: rainfall and termite engineering. In the complete model described above (which includes the feedback between termite and vegetation dynamics and the asymmetric root-system growth), there are two important simplifications. First, despite its stochasticity, the *average* rainfall levels provided by the rainfall function Eq.(14) remain constant along the years; in reality, however, there may be (consecutive) years of drought or higher rainfall. Second, the increased plant mortality imposed by termites on nest was arbitrarily fixed to a high rate to ensure depletion; in reality, mortality levels are most probably variable and even correlated with rainfall levels (e.g. if rainfall is high, there may be high water availability in the system that does not require such intense engineering to ensure water accumulation).

In order to study the dependence of the model results on these two assumptions, we studied the stationary state of the system under *i*) changes in average rainfall over a series of consecutive years, and *ii*) diverse values for the on-nest mortality, ν, and combinations of ν and rainfall average. These experiments, in turn, assess how the ecosystem as a whole (including different termite responses) behaves under different stress levels.

For the first "stress test", we first ran simulations of the system, both with and without termites, until stationarity was reached; we then simulated drought in both versions by decreasing annual rainfall inputs by 20% (per multi-model CMIP5 projections predicting 10-30% decreases in mean precipitation in southwestern Africa by 2100[66]) over durations of 1, 5, and 10 consecutive years before returning rainfall to baseline. In all cases, with and without termites, the original vegetation pattern re-emerged following drought. Importantly, however, the presence of termites increased both ecosystem resistance (i.e., less vegetation biomass was lost) and recovery (i.e., original pattern re-emerged much more rapidly) to extended drought (rate of recovery was similar for one year of drought, but approximately five-times faster in the +termite system following a decade of drought) (see Supplementary Video 4).

The second test involved variations of termite-induced mortality to study how that affects the emergent stationary state for the system. Values of ν below 1.25 (i.e. enhancement of mortality below 25% with respect to plant natural mortality) result in stationary states with similar matrix vegetation patterns, but smaller, more irregular FCs with additional inner vegetation clumps. In

other words, mortality is not sufficiently enhanced for the on- nest areas to show a clean bare disc. For ν above 1.25, discs are clean and the FCs are well defined. Values of ν around the 1.25 threshold show a combination of completely-bare discs and irregular FCs with isolated inner clumps. This threshold changes when average rainfall levels change (for higher average rainfall, higher mortality enhancement is needed to keep clean bare discs on nests) (see Extended Data Fig. 7). This may explain why similar species of termites can produce different-looking landscape effects depending on their geographic location[17].

4. Data and Analysis

4.1 Insect-nest distributions

We used high-resolution satellite imagery to quantitatively analyze the spatial distribution of social-insect nests in four countries on three continents (termite mounds in Kenya, Mozambique, Brazil, and Australia, and harvester ant nests in the USA). In all cases, these features were clearly distinguishable in imagery (Fig. 1, Extended Data Fig. 3) and the identities of the insect species that built them have been unambiguously established in published field studies. We selected the African examples because they occur in long-term field study sites where members of our team (RMP, CET, TCC, JAG, RAL) have for years studied various aspects of ecology, including termite mounds[3,4]. We selected the examples from North and South America semi-arbitrarily to expand (a) the global extent of our dataset, (b) the diversity of mound physiognomies (from 5-m tall hills covered by woody thickets to low domes covered by grasses, to shallow bare areas that strikingly resemble Namibian FCs), and (c) the taxonomic breadth of social-insect species responsible for building them (different termite subfamilies in Africa vs. Brazil, ants in North America). We further re-analyzed the Namibian FC sites of[10] to ensure concordance and comparability with our other analyses. Finally, we examined aerial photographs from a fourth continent, Australia, where *Amitermes* sp. (Termitidae) mounds occur in similar configurations (Extended Data Fig. 3); however, their geometry makes them less reliably visible in satellite imagery, which constrained us to aerial parallax photographs that could not be scaled and georeferenced and thus allowed for only one type of spatial analysis (Voronoi diagram, see below).

Kenya. Mounds built by the termite *Odontotermes montanus* (Macrotermitinae) are widespread in the Kenyan highlands and have been described by Darlington[67] as "large lenticular or conical mounds of soil [that] occur in characteristically overdispersed (evenly-spaced) patterns over large areas of Africa [and that] may be bare or well-vegetated, but always have a different flora and soil (texture and chemistry) from their surroundings." These mounds are typically "clearly visible from the air because the vegetation on them is different in color and texture from that between mounds"[68]. This description applies to the mounds at our long-term field study site, Mpala Research Centre (~0°17'51" N, 36°51' E) in Laikipia, central Kenya. The *O. montanus* mounds at this site have been intensively studied, including repeated ground-truthing and excavation of mound locations deduced from satellite imagery[3,69-71]. We analyzed two topographically and edaphically homogeneous rectangular areas at Mpala (areas mapped = 0.975 km^2 and 1.201 km^2, comprising 205 and 241 mounds, respectively) using multispectral QuickBird satellite imagery from July 2013 (Fig. 1b, Extended Data Fig. 3).

Mozambique. Our second long-term field site is Gorongosa National Park (~18°57' S, 34°21' E) in Sofala, Mozambique. There, nests built by *Macrotermes mossambicus* and *M. subhyalinus* (Macrotermitinae) occur as large hills (3-m tall on average, and up to 6 m) that support woody vegetation thickets with distinctive species composition. These mounds were extensively described by Tinley[72] (p. 75): "Their impact on the landscape is most clearly seen from the air. The dots of their evenly spaced hills are made conspicuous either by being bare (in desertic areas especially), or covered in thicket clumps" of ~20-m diameter. In Gorongosa, we analyzed a subsection from a 0.630-km^2 rectangular area in Gorongosa National Park (~18°57' S, 34°21' E) comprising ~152 total mounds in heterogeneous *Acacia*/palm savanna, using multispectral WorldView-2 satellite imagery; this analysis was ground-truthed by comprehensively mapping all mounds within the encompassing area on foot (see *Ground surveys*, below).

Brazil. Funch[73] published qualitative field observations and representative imagery from a semi-arid region of northeastern Brazil containing "tens of millions of regularly spaced termitaria (between 2 and 4 m tall, at densities of up to 35 ha^{-1})," built by *Syntermes dirus* (Termitidae). We analyzed two areas (0.209 and 0.409 km^2, comprising ~452 and 751 mounds, respectively) from this region[73] (~12°30 S, 41°37 W), using Google Earth (Fig. 1c, Extended Data Fig. 3).

North America. Although mound-building termites are largely confined to the tropics, harvester ant (Formicidae: *Pogonomyrmex* spp.) nests in the arid western and southwestern United States are readily identifiable in satellite imagery[74] as bare unvegetated circular discs of 1–5 m diameter, often superficially resembling Namibian fairy circles[75,76]. We analyzed two areas of 0.308 and 0.179 km^2 comprising ~510 and 224 nests, respectively, in Arizona (~36°15 N, 113°05' W) as described by Sparavigna[76], using Google Earth (Fig. 1d, Extended Data Fig. 3).

Namibia. We analyzed the distribution of FCs at three Namib Desert sites within the Giribes Plain (G) and Marienfluss Valley (MV) sites in the same rectangular areas analyzed in recent work[10], with aerial extents of 0.288 (G1), 0.294 (G2) and 0.322 km^2 (MV) and comprising 1181, 1288 and 676 FCs respectively, using Google Earth (Fig. 1f, Extended Data Fig. 3).

Australia. We analyzed oblique aerial photographs (obtained from photographer Ingo Arndt) of *Amitermes* mounds in Litchfield National Park, comprising 249 and 295 mounds, respectively. The specific geographic coordinates for these images are unknown, and we were unable to analyze these mounds from satellite imagery; generic coordinates for Litchfield are ~13°17' S, 130°45' E).

Image analysis. Multispectral imagery from Kenya and Mozambique was deliberately obtained from wet and dry seasons, respectively, as this is when the spectral characteristics of mound vegetation (herbaceous and woody, respectively) are most distinct from the surrounding matrix. We created false color composite images of each site by displaying red, green, and blue colors in the near-infrared, red, and green bands, respectively, which allowed us to readily detect green vegetation. We hand-digitized the locations of all mounds in each image segment using these composite images, placing a point at the center of each mound and recording the associated geographic coordinates. Final mound maps and location data were then exported for spatial analysis. These data are available on Dryad (dryad:tbd).

For the Brazilian, North American, and Namibian sites, we did not have multispectral imagery. Instead, we utilized freely available Google Earth imagery with roughly equivalent spatial resolution, and applied the same hand-digitization approach described above.

Ground surveys. Ground-based mapping in Gorongosa National Park, Mozambique, was conducted during July 2015. We walked six adjacent 0.1 × 2 km belt transects (total contiguous area 0.6× 2 km) and comprehensively recorded the location and approximate size (estimated height, nearest 0.5 m) of every termite mound using a hand-held GPS (Oregon 600, Garmin). For our final analysis we excluded mounds of height ≤ 1m, which we categorized as immature/incipient mounds.

Quantitative analysis of termite-mound distributions

We analyzed the spatial distribution of termite mounds, ant nests, and fairy circles (henceforth, "points") using the mound maps and associated location data described above, and compared these to the patterns of mound distribution generated by our model. If the rectangular areas of the maps were not aligned with the north-south axis, due to natural barriers (riverbeds, topographical reliefs), we rotated them to a north-south orientation (using MATLAB).

Similarly to the analysis performed for the model, we calculated PCFs and Ripley's *L* functions for each different area (see section 1.1). In all cases, the data indicated regularity at distances corresponding to the distances between neighbors that were calculated from Voronoi tessellations[40] (see Extended Data Fig. 4). We computed Voronoi tessellations for the point patterns, from which we extracted the following information: (1) distributions of nearest-neighbor numbers for each point, i.e., the number of corners of each Voronoi tile, which provides information on the regularity of the pattern (Fig. 1g, Extended Data Fig. 3); (2) distributions of tile areas (mean area and coefficient of variation); and (3) distributions of the distances of all points to their nearest neighbor (after[10]). Following[10], we removed all edge tiles with corners touching the borders of the analyzed area for these analyses. Therefore, the effective number of mounds analyzed for each area was smaller than the total number of mounds present.

4.2 Spatial vegetation patterns

We collected low-altitude aerial imagery of Namibian FC and matrix vegetation at the Namib Rand Nature Reserve (NRNR) in southern Namibia (25.04º E, 15.94º S), where fairy circles have been intensively studied and biotic/abiotic conditions are well characterized[6,7,12]. Mean annual precipitation is 70-80 mm[6], with most rainfall occurring from December-May. The site consists of red Kalahari sand plains and dunes typical of the habitat in which fairy circles are found in southwestern Africa[6,7]. The flora is co-dominated by three congeneric grass species: *Stipagrostis obtusa*, *S. uniplumis*, and *S. ciliata*[12]. In February 2015, we identified 10 sites spanning ~35km of suitable fairy circle habitat within NRNR. At each site, we haphazardly selected 10 pairs of fairy circles and measured the distance between circles (from outer ring edge to outer ring edge) and the size (average of two perpendicular diameters within the vegetation ring) of each FC. The density and size of FCs varies across this landscape[6]; the mean (± SEM) diameter of FCs in our dataset was 5.94 ± 0.23 m, and the mean distance between circles was 6.9 ± 0.4 m.

760 Imagery was collected using an approach similar to that described in[4] at a subset of our sites: the
761 most northern (24.94º E, 25.95º S), the most southern (25.25º E, 16.02º S), and the most central
762 (25.13º E, 16.01º S). We photographed matrix vegetation at the midpoint between 30 pairs of
763 neighboring FCs (n = 10 pairs per site; Fig. 4b). Leaf litter was manually removed prior to
764 imaging to reduce dead plant material that might otherwise have obscured spatial patterns in
765 standing vegetation. Images were recorded using a digital camera (Canon PowerShot S110),
766 which was mounted on an 11-m carbon-fiber pole (Ron Thompson Gangster Carp Pole),
767 mounted such that it could be held parallel to the ground at 10-m height. Exposure was
768 controlled manually to maintain consistency in changing light conditions. For all images, this
769 camera rig was held at constant height by the same individual (TCC). A reference object was
770 placed in all images and used to scale them to a pixel size of 0.333 cm.
771
772 Analysis of spatial vegetation pattern

773 Images were scaled and a large rectangular sub-area of similar size (1340 × 1340 pixels for two
774 sites, and 900 × 900 pixels for a site in which fairy circle density was higher) was selected from
775 each image to comprise only grass and soil (i.e., no fairy circles) and no visible disturbance
776 (n=27, three of the images were excluded because they did not have a large enough area between
777 circles). We transformed RGB (red green blue) images to HSV (hue saturation value) and
778 digitized the images into binary representations of the vegetation vs. soil based on the saturation
779 channel.
780
781 For comparison with the model simulations with stochastic seasonal rainfall, we selected
782 snapshots of the simulated vegetation in the wet season in different years (we used snapshots
783 from February, corresponding to when the field images were collected in 2015). From these
784 snapshots, we selected 2 subsections (73 × 73 and 135 × 135 pixels) between neighboring FCs (n
785 = 52, 26 years × 2 subsections year^{-1}). We transformed the patterns of biomass density from the
786 model into binary images (vegetation vs. bare soil; see Fig. 4c) according to a lower threshold
787 found from temporal and spatial analyses of the model data (0.015 Kg/m^2).
788
789 ***Analysis of spatial frequencies.*** We used the two-dimensional (2D) Fourier transform and a
790 subsequent computation of the 2D periodogram (i.e., power spectrum[42]), to provide a
791 quantitative characterization of the spatial patterns[43]. The amplitude values of the periodogram
792 are a measure of the explicit spatial frequencies in the image. We then calculated the radial
793 spectrum $\boldsymbol{r}$ (sum of the periodogram values on concentric ring-shaped regions of the 2D surface),
794 to quantify the portion of image variances that can be accounted for by a simple cosine wave
795 repeating itself r times (wavenumber) along a travel direction of the periodogram.
796
797 We normalized the radial spectra for: (a) wavenumber, by dividing $\boldsymbol{r}$ by the size of the domain in
798 the analyzed image (ca. 4.45 and 3 m for field images and 3.65 to 6.75 m for simulations); and
799 (b) amplitude of the radial spectrum, by dividing by the maximum of the mean.
800
801 We show that the spatial frequencies of the simulated vegetation patterns agree with the
802 characteristic spatial frequencies in the vegetation pattern in our field site, as shown by a peak of
803 the radial spectrum at ca. 2 cycles m^{-1} (Fig. 4d). Furthermore, the shape of the radial spectrum,
804 the peak of the mean standardized $\boldsymbol{r}$-spectrum at a low wavenumber and the fat tail, is
805 characteristic of a spotted pattern[77].

61. Hu, J., Zhong, J. H. & Guo, M. F. Alate dispersal distances of the black-winged subterranean termite *Odontotermes formosanus* (Isoptera: Termitidae) in southern China. *Sociobiology* **50,** 513–520 (2007).
62. Mullins, A. J. *et al.* Dispersal flights of the Formosan subterranean termite (Isoptera: Rhinotermitidae). *J. Econ. Entom.* **108,** 707–719 (2015).
63. Sileshi, G. W., Arshad, M. A., Konaté, S. & Nkunika, P. O. Termite-induced heterogeneity in African savanna vegetation: mechanisms and patterns. *J. Veg. Sci.* **21,** 923–937 (2010).
64. Darlington, J. P. Arena nests built by termites in the Masai Mara, Kenya. *J. East Afr. Nat. Hist.* **96,** 73–81 (2007).
65. Rietkerk, M. *et al.* Self-organization of vegetation in arid ecosystems. *Am. Nat.* **160,** 524–530 (2002).
66. Collins, M. R. *et al*. Long-term Climate Change: Projections, Commitments and Irreversibility. In: Stocker, T.F., D. Qin, G.-K. Plattner, M. Tignor, S.K. Allen, J. Boschung, A. Nauels, Y. Xia, V. Bex and P.M. Midgley (eds.), *Climate Change 2013: The Physical Science Basis. Contribution of Working Group I to the Fifth Assessment Report of the Intergovernmental Panel on Climate Change*. Cambridge University Press, Cambridge, United Kingdom (2013).
67. Darlington, J. P. E. C. Lenticular soil mounds in the Kenya highlands. *Oecologia* **66,** 116–121 (1985).
68. Darlington, J. P. E. C. & Bagine, R. K. N. Large termite nests in a moundfield on the Embakasi Plain, Kenya (Isoptera: Termitidae). *Sociobiology* **33,** 215–225 (1999).
69. Palmer, T. M. Spatial habitat heterogeneity influences competition and coexistence in an African acacia ant guild. *Ecology* **84,** 2843–2855 (2003).
70. Brody, A. K., Palmer, T. M., Fox-Dobbs, K. & Doak, D. F. Termites, vertebrate herbivores, and the fruiting success of *Acacia drepanolobium*. *Ecology* **91,** 399–407 (2010).
71. Fox-Dobbs, K., Doak, D. F., Brody, A. K. & Palmer, T. M. Termites create spatial structure and govern ecosystem function by affecting N_2 fixation in an East African savanna. *Ecology* **91,** 1296–1307 (2010).
72. Tinley, K. L. Framework of the Gorongosa Ecosystem. Ph.D. thesis, University of Pretoria, South Africa (1977).
73. Funch, R. R. Termite mounds as dominant land forms in semiarid northeastern Brazil. *J. Arid Environ.* **122,** 27–29 (2015).
74. Fletcher, R. S., Everitt, J. H. & Drawe, L. Detecting red harvester ant mounds with panchromatic QuickBird imagery. *J. Appl. Rem. Sens.* **1,** 013556 (2007).
75. Dibner, R. R., Doak, D. F. & Lombardi, E. M. An ecological engineer maintains consistent spatial patterning, with implications for community-wide effects. *Ecosphere* **6,** 151 (2015).
76. Sparavigna, A. C. Patterned vegetation created by red harvester ants and evidenced in satellite images. *HAL* hal-01289240 (2016).
77. Barbier, N., Couteron, P., Lejoly, J., Deblauwe, V. & Lejeune, O. Self-organized vegetation patterning as a fingerprint of climate and human impact on semi-arid ecosystems. *J. Ecol.* **94,** 537–547 (2006).

Supplementary Videos Captions

Supplementary Video 1. Dynamics of the termite model. Pink dots represent the center of young (incipient) colonies; blue dots represent the center of mature (established) colonies. Pale blue = foraging territory; darker blue = territory boundary.

Supplementary Video 2. Dynamics of the termite-vegetation model from initial state to stationarity. Starting with a single colony and a homogeneous distribution of vegetation, the coupled system self-organizes to patterned vegetation and regularly-organized FCs. The birth and death of colonies marks the emergence and disappearance of FCs. The bottom panel shows the rainfall availability (orange = data-inferred function; red point = instantaneous value of the stochastic rainfall function; grey = historical rainfall within the year). The middle panel, shows the dynamics of termite territories, which influence (and are influenced by) the dynamics of vegetation (top panel). Note the gaps matching the location of the centers; they are surrounded by taller vegetation, which defines the FCs.

Supplementary Video 3. Close-up view of the coupled dynamics of colonies and vegetation from initial state to stationarity, focused on the matrix vegetation. Territories expand and coexist, giving rise to neighboring FCs. Shrinkage of territories due to competition gives the opportunity for young colonies to establish in the available space. Matrix vegetation self-organizes in response to scale-dependent feedbacks along the differences in soil moisture induced by the FCs. Panels are same as in Supplementary Video 2.

Supplementary Video 4. Comparison of the response of coupled (left) and pure-SDF (right) systems to 10 consecutive dry years (20% reduction of average rainfall) followed by return to baseline rainfall. The same reduction in rainfall leads the SDF system to almost complete extinction of vegetation, which remains in densities that are much lower than in the FC case. After rainfall returns to baseline, vegetation in both systems recovers, but the FC ecosystem is fully restored to stationarity much faster than the SDF system. After the FC system reaches stationarity, the video focuses on only the pure-SDF system. For both systems, dry years are represented by blue lines in the rainfall function plot; baseline years are represented by grey lines. Snapshots taken the same month each year, represented by the red point on the rainfall (bottom) panel.

Extended Data Table 1.

List of parameters for the termite model and associated literature sources and estimation procedures.

Symbol	Description	Value	Units	Source
R_{max}	Maximum foraging radius	30	m	25-30m for subterranean termites and 15m for another Namib desert species in FC landscapes[44]; median distance of 35m for a desert rhinotermitid (*Heterotermes aureus*)[45]
B_{max}	Maximum possible colony biomass (carrying capacity)	$B_{ind}\times(2\times10^{6})$	g (termite)	Estimates for other Rhinotermitidae species from diverse habitats include >300,000 [46], >800,000 [47], to >2 and >3 million[48].
B_{mat}	Maturity/reproduction threshold	$B_{max}\times0.5$	g (termite)	Chosen as half $B_{\max}$ [31]. This choice does not influence results.
B_{ind}	Biomass of individual termite	2×10^{-3}	g (termite) individual^{-1}	Within weight range reported for various Rhinotermitidae spp.:[49-51].
c	Biomass conversion factor	0.07	g(termite) g^{-1}(res)	Tables 9.6-9.8 [50].
μ	Colony population birth rate	6.00	year^{-1}	Growth rate such that max size reached in 3 years (assumed to be smaller than that of largest colony species [31]).
m	Per capita worker natural mortality rate	1.00	year^{-1}	We assume the maximum lifetime of neuters ≈ 1 year [52].
P_{cst}	(Constant) vegetation density	Varied	Kg m^{-2}	Characteristic of arid and semi-arid environments[53].
m_C	Death rate of mature colonies	2.7	year^{-1}	Based on lifespan of ~25 years, which falls within the cross-taxa range for termites[37].
f_A	Alate production factor as proportion of $B_i(t)$	0.1	-	Within the cross-taxa range (0.012 – 1.42)[50] (their Table 9.7)
α	Reference value, conflict outcome probability	1.05	-	Unknown. Chosen to ensure that wars result in coexistence only when colonies have very similar sizes (based on the assumption that the war is a "war of attrition"[29,35,54]).
β	Shape factor for conflict outcome probability	150.00	-	
α_2	Reference value for conflict probability	2.25	-	Unknown. Chosen to accentuate the difference in expansionistic tendencies as a function of colony size.
β_2	Shape factor for conflict probability	10.00	-	
q	Shrinking factor for small winning colonies	0.1	-	Unknown. Chosen to be small but does not affect qualitative behavior.
A_{min}	Minimum viable area for a colony	$\pi\times0.1^{2}$	m^{2}	Arbitrary low number chosen for computational convenience.
f_m	Fraction of foraging territory occupied by mound proper	0.5	-	Approximate value based on data on foraging activity in *P. allocerus*[7].
ν	On-mound plant mortality enhancement	5.00	-	Chosen to simulate high mortality and low density of plants within fairy circles.
m_P	Vegetation mortality	10.00	year^{-1}	Chosen to fit tussock grasses for continuity with merged model (Extended Data Table 2).
N	Lateral grid size	1024	sites	Chosen for computational convenience.
dt	Integration time step	1	year	Chosen due to seasonality of the Namib desert
dx, dy	Mesh sizes	0.05	m	Chosen for computational convenience.

Extended Data Table 2.

List of parameters for the vegetation parts of the merged model and associated literature sources.

Symbol	Description	Value	Units	Source
K	Maximum standing biomass density	0.50	Kg m^{-2}	[55]
m_P	Vegetation natural mortality rate	10	$year^{-1}$	[9]
γ	Maximum infiltration rate	40	$year^{-1}$	[15]
Q	Infiltration half-saturation constant	0.1	Kg m^{-2}	[15]
W_0	Infiltration contrast between bare and vegetated soil	0.9	-	[10,15]
N	Soil water evaporation rate	4	$year^{-1}$	[15]
R_{educ}	Evaporation reduction due to shading	0.75	-	Within the range [10,15]
D_P	Seed dispersal coefficient	$3x10^{-3}$	$m^2 year^{-1}$	[56,57]
D_W	Soil water diffusivity	$5x10^{-3}$	$m^2 year^{-1}$	[58]; personal comm.: Ignacio Rodriguez-Iturbe.
D_O	Surface water diffusivity	0.00	$m^2 year^{-1}$	No topography + sandy soils (water infiltrates very quickly); personal comm.: Ignacio Rodriguez-Iturbe.
S_0	Minimal root system size	0.04	m	[59]
E	Root augmentation per unit biomass	4.0	Kg^{-1} m^2	[60]
Λ	Plant growth rate per unit soil water	0.25	Kg^{-1} $m^2 year^{-1}$	~10 times larger than value used for shrubs [15] since grasses grow more efficiently.
Γ	Soil water uptake per unit plant biomass	12	Kg^{-1} $m^2 year^{-1}$	[9,60]
R_0	Rainfall function reference parameter	54	mm $year^{-1}$	Chosen to match rainfall levels and variability shown by our data compilation.
ω	Rainfall function shape factor	1.0	-	
σ_R	Rainfall noise standard deviation	$2.5x10^{-3}$	mm $year^{-1}$	

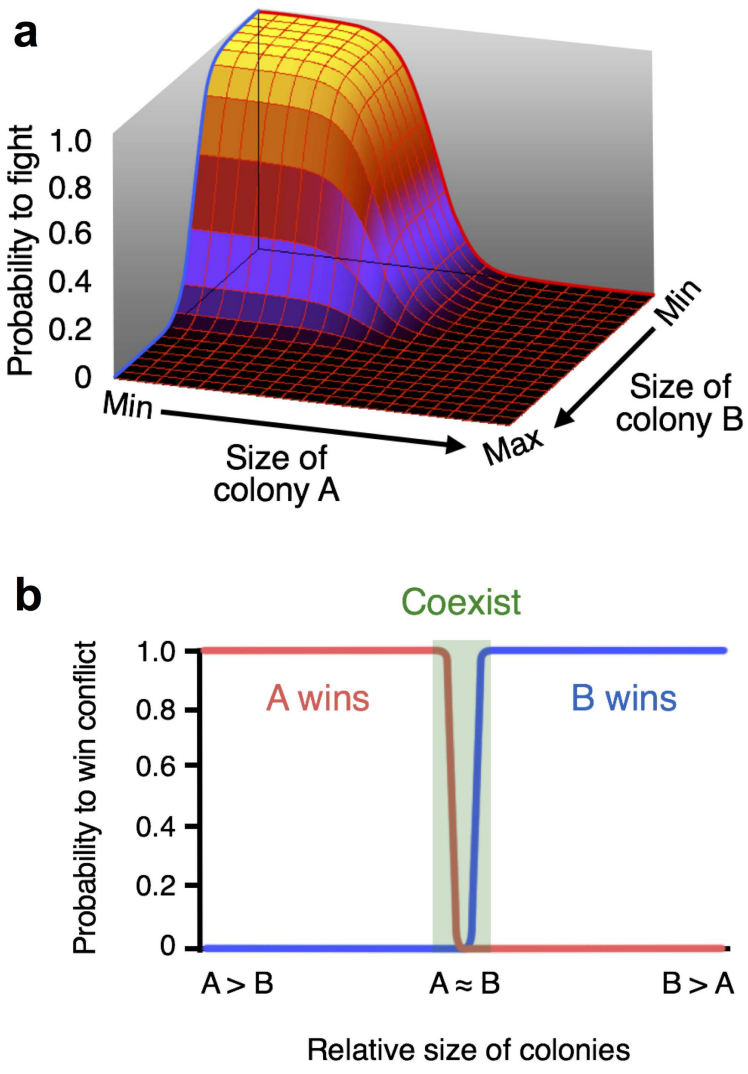
a
Probability to fight
1.0
0.8
0.6
0.4
0.2
0
Min
Size of colony A
Max
Min
Size of colony B
b
Coexist
Probability to win conflict
1.0
0.8
0.6
0.4
0.2
0
A wins
B wins
A > B
A ≈ B
B > A
Relative size of colonies

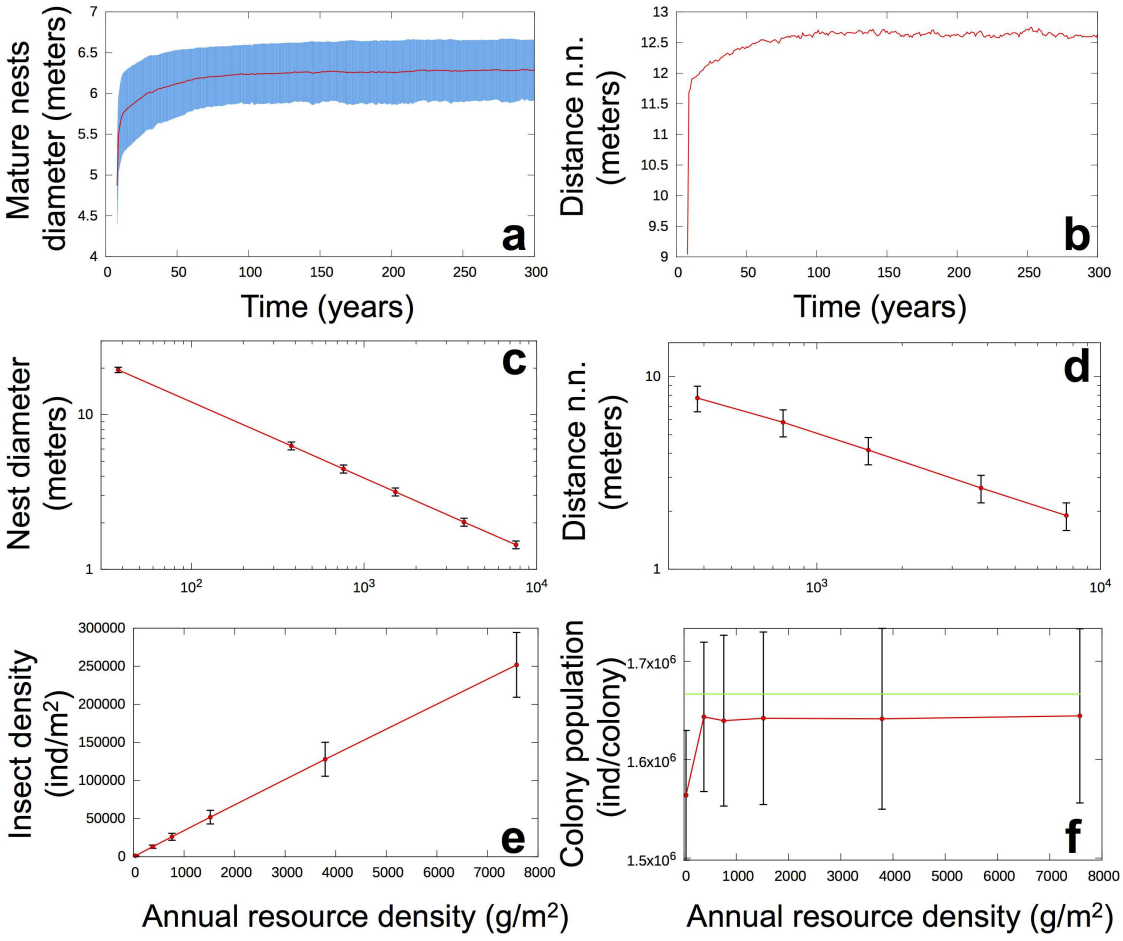
Mature nests diameter (meters)
a
Time (years)
Distance n.n. (meters)
b
Time (years)
Nest diameter (meters)
c
Distance n.n. (meters)
d
Insect density (ind/m²)
e
Annual resource density (g/m²)
Colony population (ind/colony)
f
Annual resource density (g/m²)

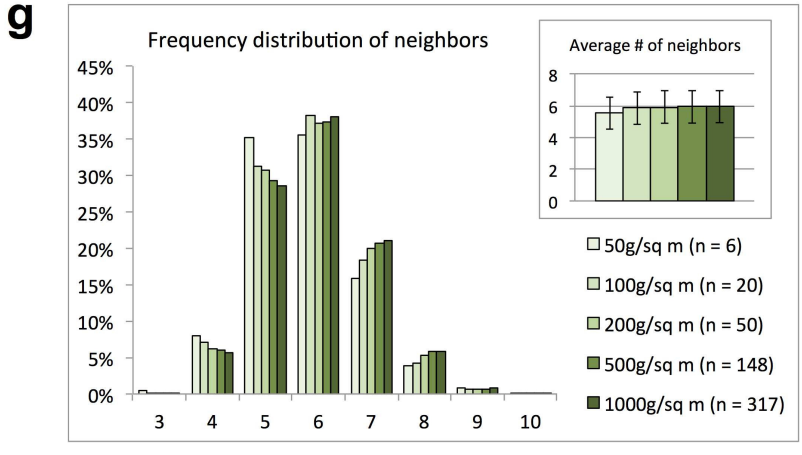
g
Frequency distribution of neighbors
Average # of neighbors
50g/sq m (n = 6)
100g/sq m (n = 20)
200g/sq m (n = 50)
500g/sq m (n = 148)
1000g/sq m (n = 317)

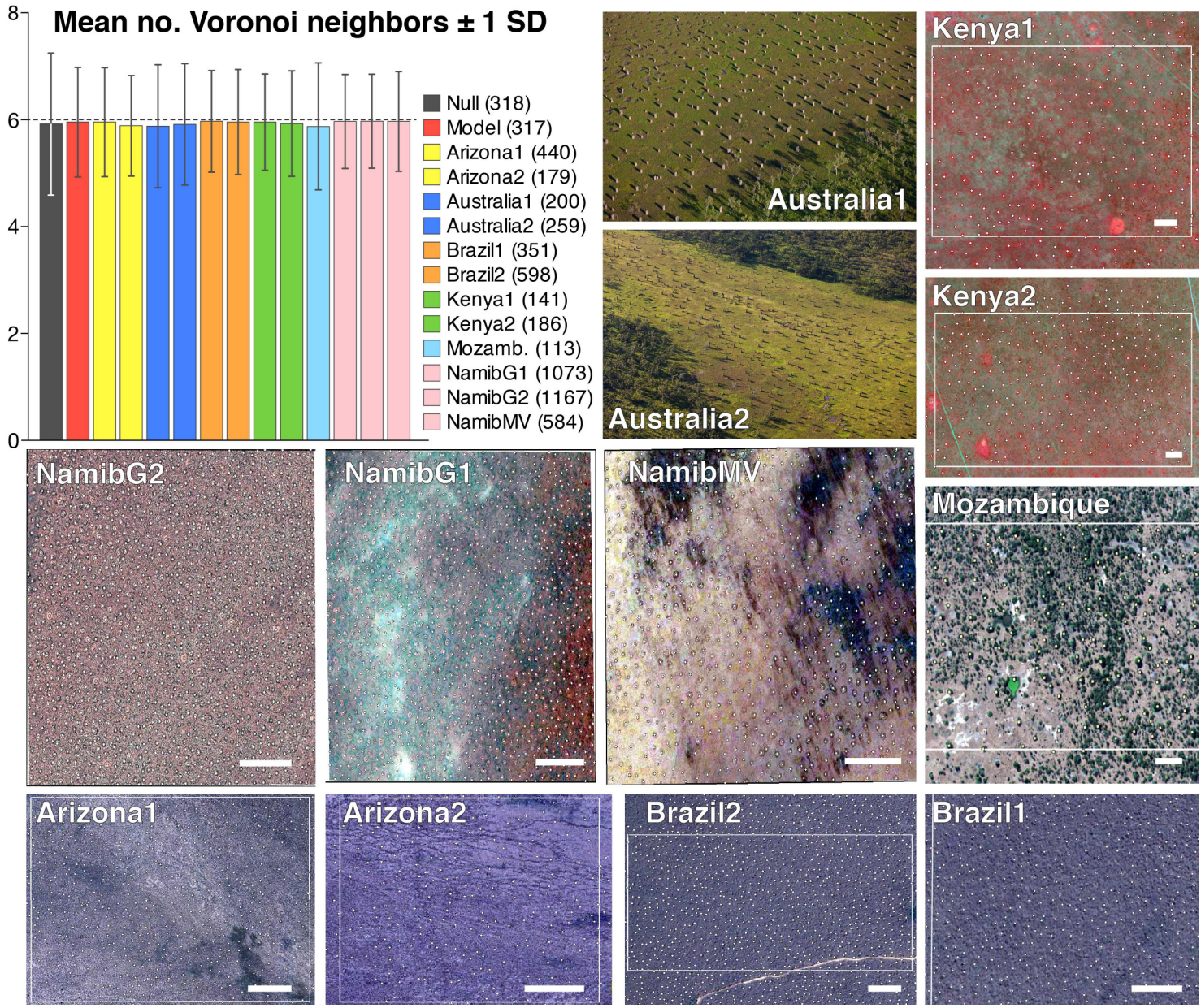
Mean no. Voronoi neighbors ± 1 SD
8
6
4
2
0
Null (318)
Model (317)
Arizona1 (440)
Arizona2 (179)
Australia1 (200)
Australia2 (259)
Brazil1 (351)
Brazil2 (598)
Kenya1 (141)
Kenya2 (186)
Mozamb. (113)
NamibG1 (1073)
NamibG2 (1167)
NamibMV (584)
Australia1
Australia2
Kenya1
Kenya2
Mozambique
NamibG2
NamibG1
NamibMV
Arizona1
Arizona2
Brazil2
Brazil1

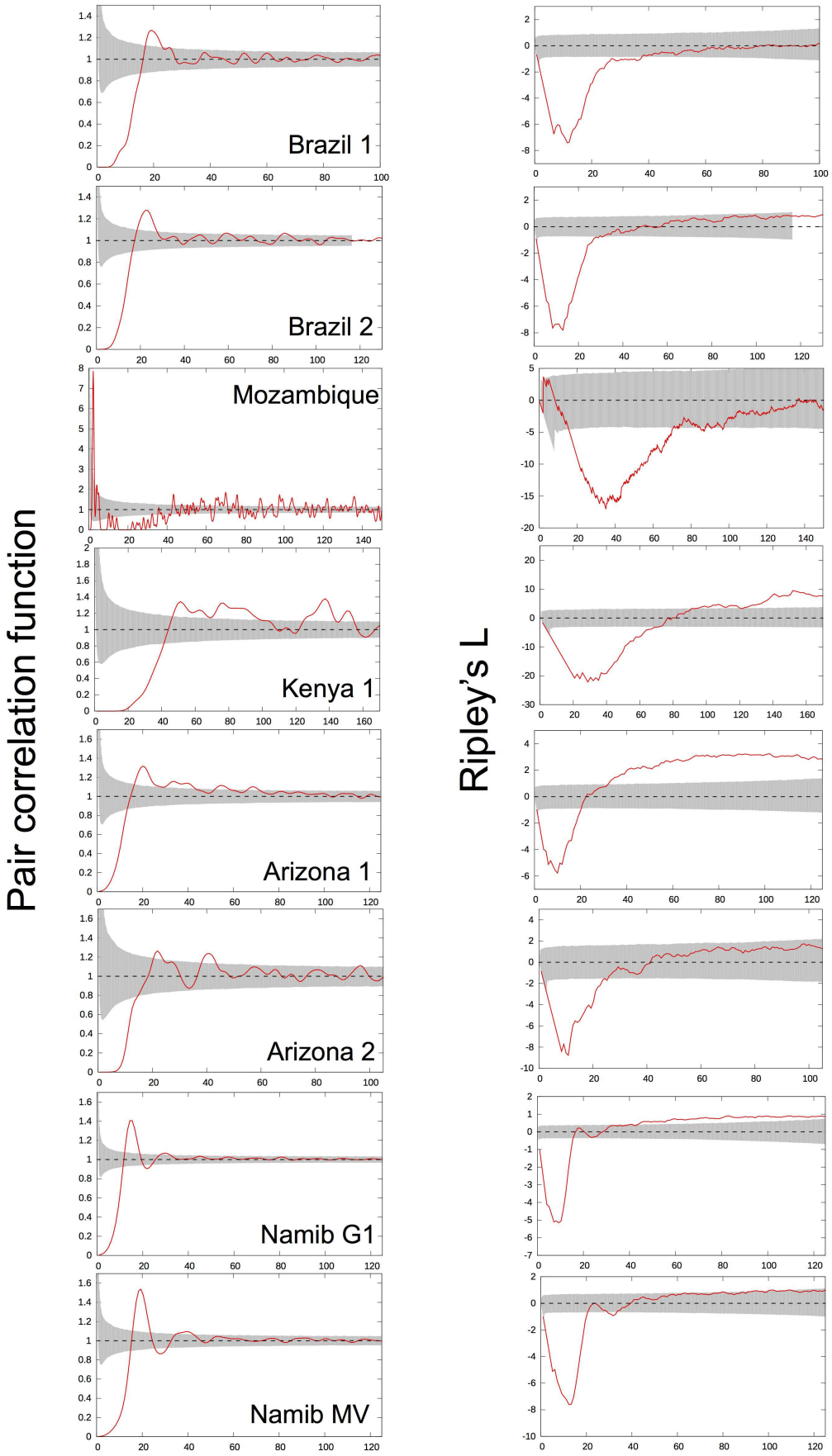
Pair correlation function
Ripley's L
Brazil 1
Brazil 2
Mozambique
Kenya 1
Arizona 1
Arizona 2
Namib G1
Namib MV

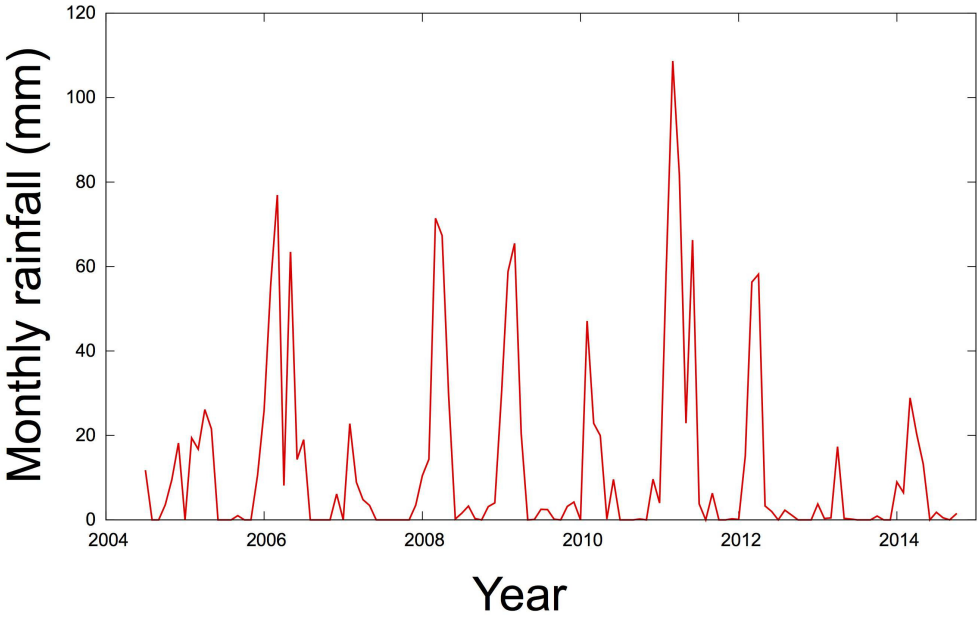
Monthly rainfall (mm)
120
100
80
60
40
20
0
2004
2006
2008
2010
2012
2014
Year

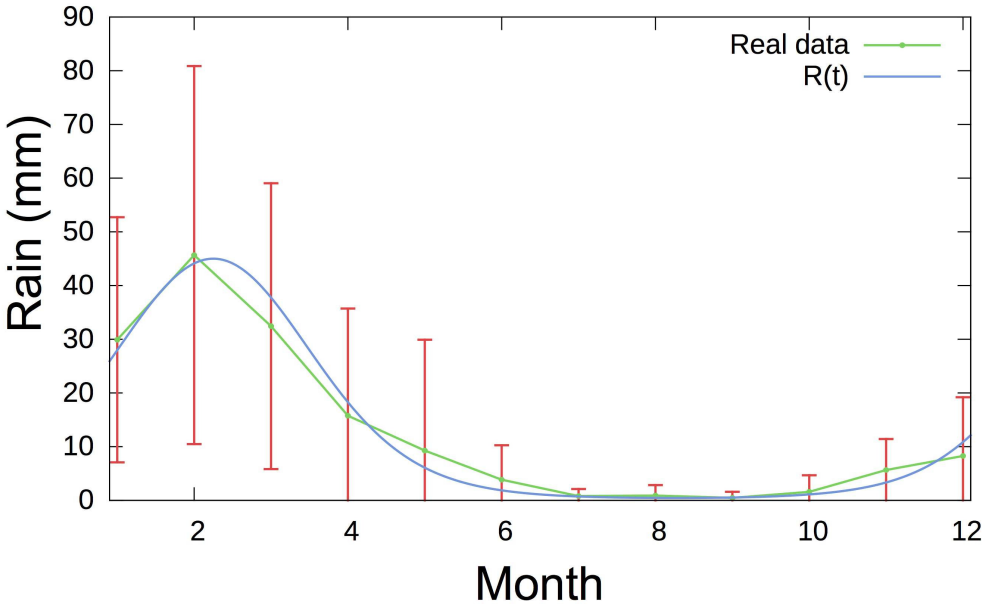
Rain (mm)
90
80
70
60
50
40
30
20
10
0
2
4
6
8
10
12
Month
Real data
R(t)

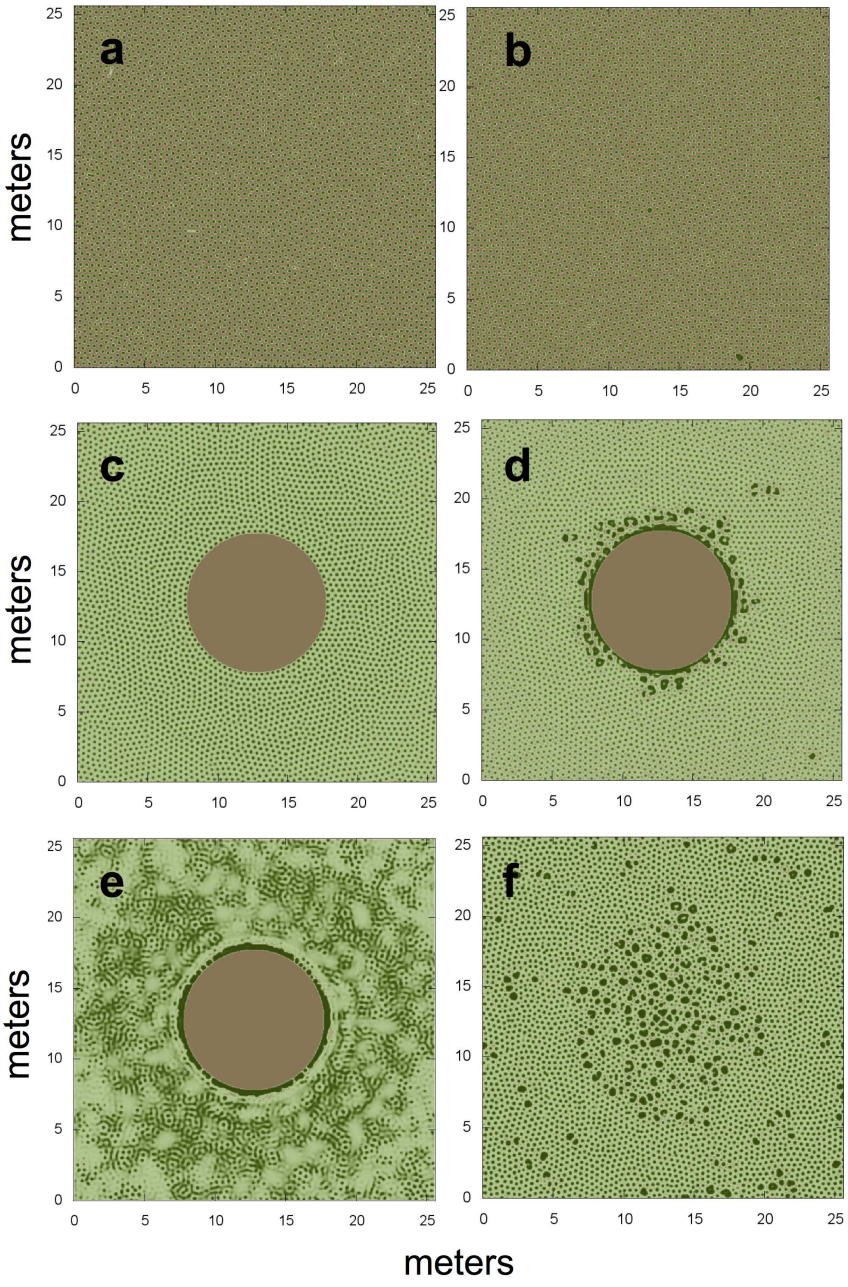
a
b
c
d
e
f
meters
meters
0
5
10
15
20
25

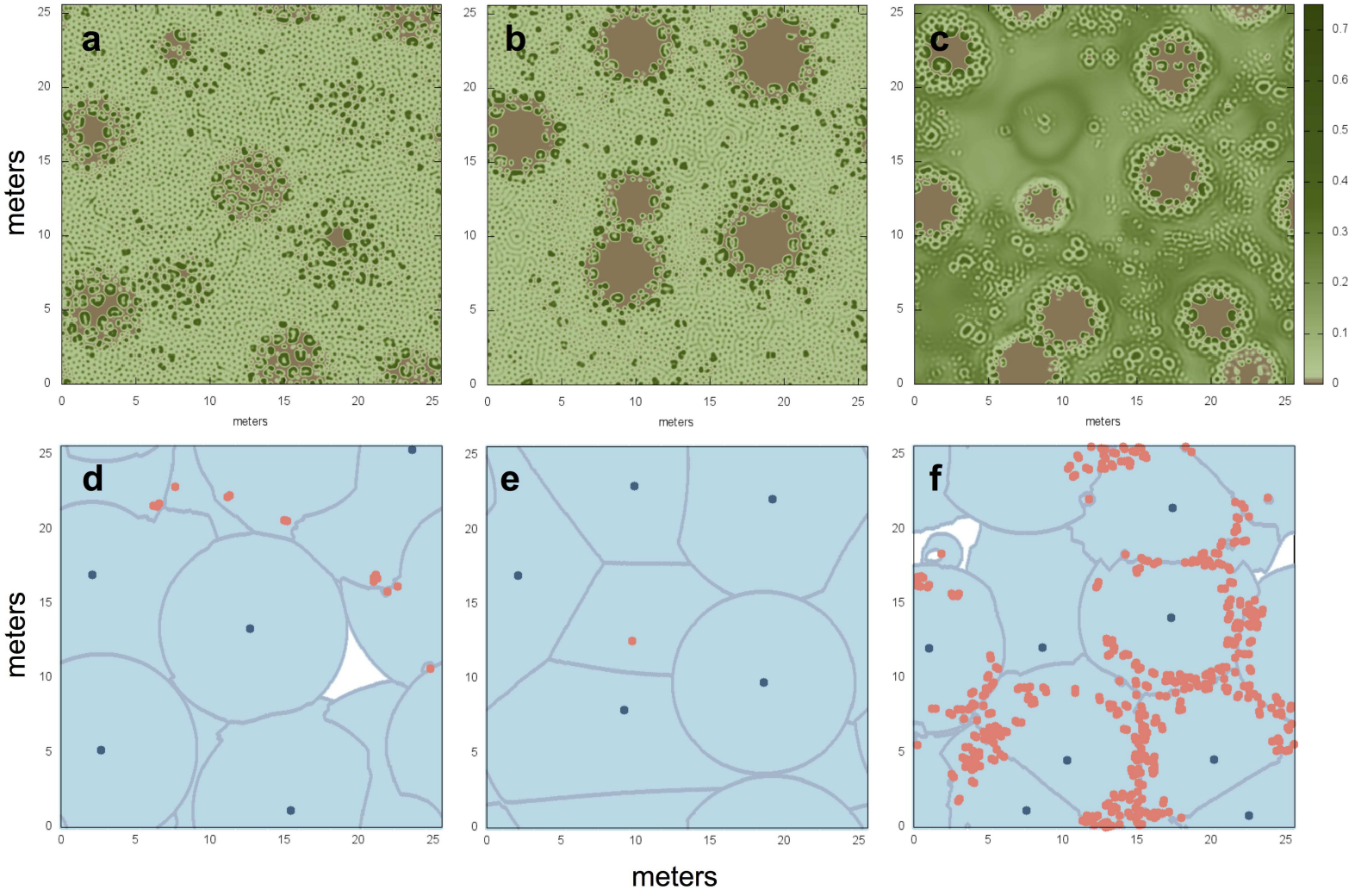
a
b
c
d
e
f
meters
meters
meters
meters
meters
0
5
10
15
20
25
0.7
0.6
0.5
0.4
0.3
0.2
0.1
0

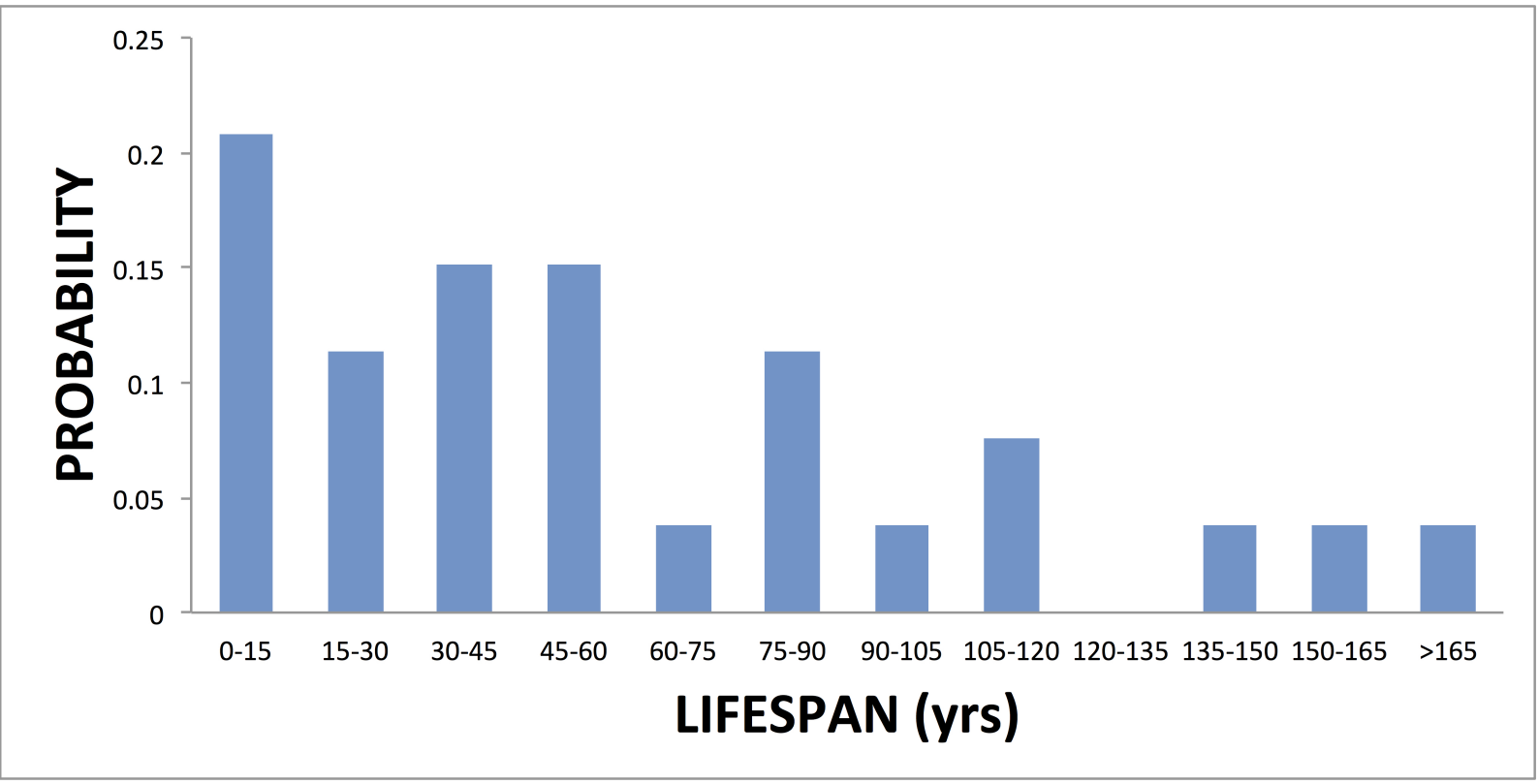
PROBABILITY
0.25
0.2
0.15
0.1
0.05
0
0-15
15-30
30-45
45-60
60-75
75-90
90-105
105-120
120-135
135-150
150-165
>165
LIFESPAN (yrs)